https://doi.org/10.5194/egusphere-2025-6253
Preprint. Discussion started: 19 January 2026

Graupel and increased turbulence observed near small-scale intermittent lightning discharges at the top of intense thunderstorms

Reinaart van Loon[1,5], Jelle D. Assink[1], Olaf Scholten[2,3], Brian M. Hare[2,3], Hidde Leijnse[1], and Aarnout J. van Delden[4]

[1]Royal Netherlands Meteorological Institute, De Bilt, The Netherlands
[2]University Groningen, Kapteyn Astronomical Institute, Groningen, The Netherlands
[3]Netherlands Institute of Radio Astronomy (ASTRON), Dwingeloo, The Netherlands
[4]Institute of Marine & Atmospheric Research Utrecht, Utrecht University, The Netherlands
[5]Wageningen University & Research (WUR), Wageningen, The Netherlands (current position)

Correspondence: Reinaart van Loon (reinaart.vanloon@wur.nl)

Abstract. Sparkles are defined as intermittent, small-scale lightning discharges near the top of thunderstorms. To increase the understanding of mechanisms that lead to sparkles, we compare high resolution lighting data from the LOw Frequency ARray (LOFAR) to data from a meteorological radar. The study focuses on the thunderstorms that crossed the northeast of the Netherlands on June 18, 2021. We used a two-stage clustering approach to computationally distinguish sparkles from other lightning structures. Subsequently, we compare the radar data near sparkles to radar data near other lightning structures. The two convective systems that produced sparkles resemble, respectively, a supercell and a squall line. Consistent with previous studies, we find that sparkles were present at high altitudes when radar reflectivity values were relatively high. Such values are associated with strong updrafts, lofting of graupel, and overshooting cloud tops. We confirm with a fuzzy-logic hydrometeor classification algorithm that graupel is often present near sparkles. Given the altitude of the radar data, the findings support the hypothesis that sparkles are caused by large charged hydrometeors that get lofted to relatively high altitudes and near a stratospheric charged screening layer. Near sparkles, radar data also shows enhanced spectral width values and heterogeneous patterns in the radial velocity. This likely represents enhanced turbulence. Our observations match hypotheses to explain the small extent of sparkles, namely folding of a charged screening layer, and fragmentation of existing charge pockets. Additionally, we hypothesize that inductive charging, enhanced by turbulence, could play a role in the formation of sparkles.

1 Introduction

The LOw Frequency ARray (LOFAR) is a radio telescope that is in use for astronomical observations and consists of numerous radio antenna fields, of which the core is situated in the northernmost part of The Netherlands (van Haarlem et al., 2013). Previous studies have shown that LOFAR antennas can detect electromagnetic signals from lightning. By correlating the observations at the various antenna fields, 4-dimensional (spatial and temporal), high-resolution images can be constructed of "Very High Frequency" (VHF) point sources (Hare et al., 2018). This methodology has been exploited to study a large variety of lighting structures with much detail (Hare et al., 2019; Scholten et al., 2021c, a, b; Liu et al., 2022; Scholten et al., 2023).

https://doi.org/10.5194/egusphere-2025-6253
Preprint. Discussion started: 19 January 2026

In order to introduce the LOFAR lightning images and to illustrate some of the visible lighting structures, Fig. 1 shows part of the LOFAR image at 19:54:22 UTC on June 18 2021. Annotations with numbering 1 through 4 show some exemplary lighting structures. Annotations 2 and 4 mark negative stepped leaders (Mazur, 2016). In Fig. 1 the propagation at the end of these negative stepped leaders is clearly visible as slanted lines. Dart leaders live on previously established leader channels and therefore propagate much faster than negative stepped leaders (Mazur, 2016). They show up as nearly vertical lines in Fig. 1a. Annotation 3 marks one of the many dart leaders in this LOFAR image. Positive leader propagation is not well captured by LOFAR. However, after the positive leader has established a leader channel, other lightning activity in the same channel can reveal its location. Hare et al. (2019) use, for example, dart leaders and needle activity to locate positive leader channels. In Fig. 1, annotation 1 marks the location of a positive leader channel. It is revealed by more than 200 ms of lighting activity in a channel-like structure, followed by a dart leader at approximately 350 ms.

Besides the large lighting structures, Fig. 1 also shows many VHF sources that seem disconnected in time and space. These small lightning structures were mainly present above an altitude of 8 km and up to almost 14 km. In LOFAR images, the altitudes above 10 km are usually not much populated. However, for the thunderstorms on June 18 2021, the "cloud" of the small-scale, intermittent VHF sources persisted over multiple LOFAR images, spanning more than an hour. The observations of these small-scale, high-altitude, intermittent discharges have been described in Scholten et al. (2023) and are named "sparkles". In the same study, the authors show that sparkles have specific spatio-temporal structures. Some of the sparkles behave in a similar manner as negative stepped leaders and even exhibit dart leaders.

Observations similar to sparkles have been reported in the United States by Emersic et al. (2011), Calhoun et al. (2013) and MacGorman et al. (2017). The authors describe that small-extent, intermittent discharges occur in severe thunderstorms, above strong vertical updrafts, where the cloud tops overshoot. In this context, the authors hypothesize that these are discharges between the charged updraft and an oppositely charged screening layer around the cloud. Periodic folding of the charged screening layer due to turbulence, would be the mechanism to bring the two sources of opposite charge together, close enough for dielectric breakdown. Calhoun et al. (2013) also hypothesize that these small discharges live in small charge pockets that limits their spatial extent. Simulations by Calhoun et al. (2014) show that charge pockets may result from turbulent mixing of a heterogeneously charged updraft. However, the temporal and spatial dimensions of the charge pockets in these simulations do not match those of the small-scale lightning observations near the top of thunderclouds.

It remains unclear why the sparkles are so much smaller than more common types of lightning flashes, and how they can, at the same time, be initiated intermittently. With this in mind, we pose the following research question: *What atmospheric conditions are favorable for sparkles and what sets them apart from conditions of other lightning phenomena?*

To address this question, we compared the LOFAR data of the June 18-2021 thunderstorms with data from a polarimetric (dual-polarization) meteorological radar, located on Borkum Island, Germany. Such a radar scans the atmospheric volume and gives a signal when its outgoing radar beam scatters or reflects upon hydrometeors (water particles or drops) or other particles. The Doppler shift of the signal provides insight into the velocity spectrum of hydrometeors (Doviak et al., 1993). The different polarimetric variables can be used to deduce the location, abundance, and the type of hydrometeor(Doviak et al.,

https://doi.org/10.5194/egusphere-2025-6253
Preprint. Discussion started: 19 January 2026

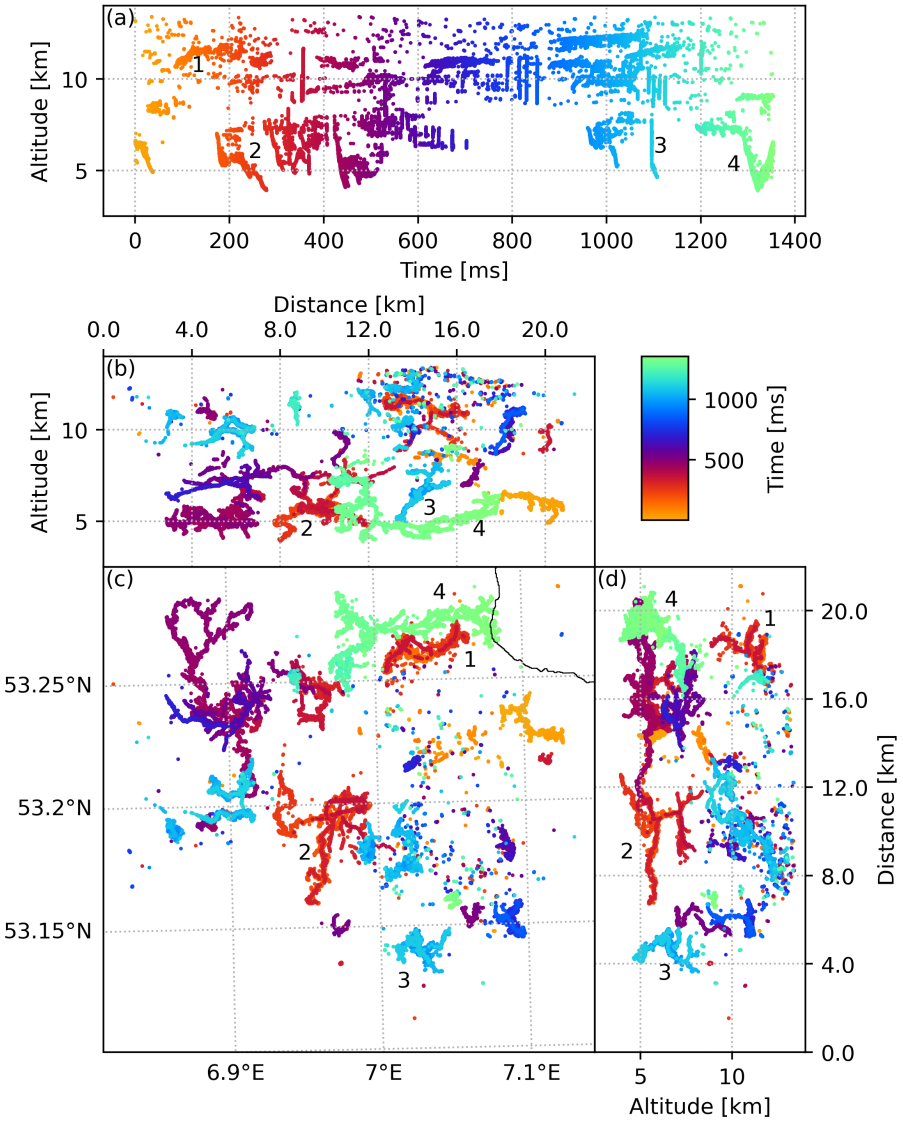

Figure 1. Part of the LOFAR image at 19:54:24 UTC on June 18, 2021. The dots show VHF point sources from lightning. The color of the VHF sources mark the timing with respect to the start of the LOFAR image. Panel (a) shows the altitude vs the timing. The bottom three panels show the projection of the VHF sources on to the planes of a three-dimensional box, a horizontal plane in panel (c) and two adjacent vertical planes in panels (b) and (d). Annotation 1: A positive leader channel. Annotation 2: A negative stepped leader. Annotation 3: A dart leader. Annotation 4: A Negative stepped leader. Sparkles are observed as a cloud of small, intermittent discharges.

https://doi.org/10.5194/egusphere-2025-6253
Preprint. Discussion started: 19 January 2026

1993; Marzano et al., 2006). With this information, it is possible to characterize storms and locate dynamical aspects such as updrafts and downdrafts (Kumjian, 2013a, b).

To gain insights in the atmospheric conditions in the vicinity of lightning, and sparkles in particular, a clustering technique is employed to find the time and locations of sparkles occurrences in the LOFAR data. The location information is used to populate statistics on radar polarimetric variables, both for (1) sparkles and (2) other lightning discharges present in the LOFAR data. These two statistical groups are subsequently compared. The results of this case study are also qualitatively compared with previous studies by Emersic et al. (2011), Calhoun et al. (2013) and MacGorman et al. (2017).

The remainder of this paper is organized as follows. Section 2 describes key aspects of the methods used in the analysis. A detailed description of the methods can be found in the Appendices. Section 3 presents the data in this study in four parts: Sect. 3.2 provides an analysis of the storm evolution and different convective systems that are observed, Sect. 3.1 presents the LOFAR data, Sect. 3.3 presents the correlations found between radar and LOFAR data, and Sect. 3.4 notes key observations, alongside exemplary figures, from visual analysis of the radar images in the context of LOFAR data. Section 4 is dedicated to the interpretation and appreciation of the results. Finally, conclusions are provided in Sect. 5.

2 Methods

2.1 LOFAR

During thunderstorms, LOFAR dumps about 2 s of raw-voltage (transient buffer) data from 6 low-band antennas (LBA) per station, from 38 Dutch stations. This data dumping takes about 15-30 minutes, thus LOFAR can record up to 10 flashes per storm. The LBAs are inverted V dipoles that are sensitive to 10-90 MHz. After recording, the data is processed into images with the "impulsive imager". This is an advanced time-of-arrival algorithm inspired by Kalman filters using cross-correlations to measure time-delays of pulses received by different antennas (Hare et al., 2018; Scholten et al., 2021d). The impulsive imager produces about 200 sources/ms with meter and nanosecond level accuracy.

2.2 Selecting Sparkles

Scholten et al. (2023) define sparkles as "spatially small (not exceeding a few 100 m) intermittent discharges near the top of the clouds where this activity is seen over extended periods lasting the full duration of a LOFAR recording." An example of a LOFAR image with sparkles is given in Section 3.1.

In order to perform a quantitative analysis, we distinguish sparkles from other lightning structures using a two-stage approach. Inspired by Fuchs et al. (2016), we apply the DBSCAN (Density Based Spatial Clustering with Noise) algorithm as implemented in Scikit-Learn (Pedregosa et al., 2011) to group VHF sources into four-dimensional lighting structures. We used visual inspection and a trial-and-error approach to find appropriate normalization constants for clustering. The normalization constants determines if two VHF sources are far apart (larger than the normalization constants) or near each other (smaller than the normalization constants).

https://doi.org/10.5194/egusphere-2025-6253
Preprint. Discussion started: 19 January 2026

In the first stage, we normalize the time and spatial coordinates of all VHF sources by dividing by normalization constants of 0.3 s and 2 km respectively. We then run DBSCAN with a minimum cluster size of 30 points, classifying each resulting cluster as "other VHF sources". Unclustered points, which are apparently not part of any large cluster, proceed to the second stage.

In the second stage, we renormalize the original time and space by dividing by 0.02 s and 200 m respectively, and now use DBSCAN with a minimum cluster size of 2 points. These clusters are classified as sparkles. Any remaining VHF sources, which were thus potentially part of sparsely imaged large clusters, are added to the "other VHF sources" category.

Finally, we reassign any sparkle VHF source to the "other VHF source" category if it is located below an altitude threshold of 8 km. This threshold removes a small number of outliers below this threshold.

The result of the sparkle classification algorithm as described above, is a categorization of each LOFAR VHF source as either a "sparkle", or as an "other VHF source".

2.3 Polarimetric Radar Data

The radar data that is used in this study comes from a polarimetric C-band radar, located on the island of Borkum in Germany. This specific radar was chosen given its favorable location and range with respect to the location of interest, i.e. the north of the Netherlands. The technical details of this radar can be found in Frech et al. (2017). The key aspects of the Borkum radar and data can be found in Appendix A.

Radar variables

In this study we use the following three radar variables: radar reflectivity (Z_h), radial velocity (V_{rad}), and velocity spectrum width (W_{rad}). Polarimetric variables are used in a hydrometeor classification (HMC) scheme to derive information about particle types in the radar measurement volume. The HMC scheme is discussed in subsection 2.3. A brief description of Z_h, V_{rad} and W_{rad} follows, but the reader is referred to Doviak et al. (1993) or Kumjian (2013a) and Kumjian (2013b) for a more thorough description.

The radar reflectivity Z_h represents the power of the radar beam that is scattered back to the radar with horizontal polarization. In this study, we do not consider the vertically polarized reflectivity Z_v. Generally, the Z_h values for a radar resolution volume are higher when there are more hydrometeors, larger hydrometeors, or hydrometeors that have a larger fraction of water with respect to ice. The shape and orientation of hydrometeors is important for the ratio between Z_h and Z_v.

The radial velocity V_{rad} is computed from the Doppler shift of the backscattered signal. It represents the velocity of the hydrometeors in the outward radial direction. Note that V_{rad} is the reflectivity-weighted mean of the velocities of all hydrometeors within a radar resolution volume (Doviak et al., 1993).

The velocity spectrum width W_{rad} represents the spread in V_{rad} within a radar resolution volume and is computed as the reflectivity-weighted standard deviation of V_{rad} (Doviak et al., 1993). Either gradients in the velocity field, potentially in the form of turbulence, or presence multiple hydrometeors with different terminal sedimentation velocities, will lead to increased W_{rad} values.

https://doi.org/10.5194/egusphere-2025-6253
Preprint. Discussion started: 19 January 2026

Hydrometeor Classification

For radar data points, the type of dominant hydrometeor is estimated using the ωradlib (Heistermann et al., 2013) fuzzy-logic hydrometeor classification (HMC) algorithm based on the method of Zrnić et al. (2001). As input, this algorithm uses polarimetric radar variables, and the conditional two-dimensional probability density functions of the following hydrometeor classifications: No Precipitation (NP), Vertically-aligned ice Crystals (VC), Horizontally-aligned ice Crystal (HC), Wet Snow (WS), Dry Snow (DS), Graupel/Hail (GH), Rain/Hail (RH), Hail (HL), Large Drops (LD), Heavy Rain (HR), Medium Rain (MR), and Light Rain (LR). The output is, per radar resolution volume and per hydrometeor type, the probability that this type of hydrometeor can explain the polarimetric radar variables. More details on HMC methods are described by Al-Sakka et al. (2013)

We classify the hydrometeor type with the highest probability as the dominant hydrometeor type for each radar point. Furthermore, the probability differences between different hydrometeor types can be used as an indication of the uncertainty of the HMC output. The radar variables considered for the HMC algorithm in this study are Z_h, differential reflectivity Z_{dr}, co-polar correlation coefficient ρ_{hv} and specific differential phase K_{dp}. The computation of the latter is described in Appendix B. In addition, we make use of ERA5 model data for temperature T. All variables are weighted equally. The conditional two-dimensional probability density functions (membership functions) are retrieved from ωradlib (2024), which are constructed based on radar signal simulations by Marzano et al. (2006).

2.4 Matching radar with LOFAR data

Throughout the analysis, the LOFAR data is compared spatially with radar data. This process involves a standard correction for the refractive index of the atmosphere (Doviak et al., 1993), georeferencing and advecting the radar data according to the ambient wind velocity, according to ERA5 reanalysis data (Hersbach et al., 2023). These steps are elaborated on in Appendix B. Note that all radar images in this work are advected to the time as indicated in the figure caption.

In this study, we compare radar data within a 2 km radius of VHF sources identified as sparkles (Section 2.2) with radar data near other VHF sources. The latter category is radar data found within a vertical column of 2 km radius of other VHF sources, but not within a 2 km radius of sparkles. A minimum altitude threshold of 8 km ensures a fair comparison of radar variables, without any potential altitude bias. A $Z_h > 0$ dB threshold ensures that we only use radar data with significant amounts of hydrometeors. Furthermore, the 0 dB threshold ensures that the signal is significantly above the noise level. Thus we do not consider the atmosphere outside clouds and clouds that are barely reflective to the Borkum radar.

https://doi.org/10.5194/egusphere-2025-6253
Preprint. Discussion started: 19 January 2026

3 Results

3.1 LOFAR data and sparkle classification

In Fig. 1a the sparkles are relatively easily distinguished as a confetti-like cloud between 8 and 12 km. Using the the algorithm and parameters described in Sect. 2.2, we find that the confetti cloud is classified as sparkles, while obvious large lightning structures are marked as other VHF sources. This is illustrated in the figures of Appendix C.

Figure 2 provides a zoom-in of the LOFAR data from Fig. 1 with the sparkles indicated as triangles with black outline. We note that there are small clusters that are not classified as sparkles. Apparently, these clusters contain more than 30 VHF sources, or multiple small (< 500 m) clusters are grouped as a single large structure by the classification algorithm. In general, this type of small clusters in the "other VHF" category, is located less than 2 km distance from clusters in the sparkle category. Taking into account the 2 km radius to select radar data near sparkles and exclusion from the subset of radar data near other VHF sources, we expect that misclassifications into the "other VHF" category will only have a marginal effect on the results.

By design, the second stage of clustering in the sparkle classification removes isolated single VHF sources from the sparkle category. We observe three types of isolated VHF sources: (1) isolated VHF sources at low altitudes < 5 km that seem to be part of larger, sparsely imaged lighting structures; (2) isolated VHF sources part of dart leaders; and (3) isolated VHF sources in or near the confetti cloud of sparkles. The latter category may be poorly imaged sparkles and can therefore be misclassified as other VHF source. However, given the 2 km radius to select sparkle data, we expect that these misclassifications will only have a marginal effect on the results. The VHF sources at low altitudes and in dart leaders (observations (1) and (2)) are rightfully classified as other VHF sources.

3.2 Storm and Lightning Overview

In our interpretation of the storm, we distinguish five different convective systems in the northeast of the Netherlands between 17:00 and 21:00, which are labeled as 'A' through 'E' in Fig. 3. The convective systems are primarily inferred from radar reflectivity (Z_h) values. The approximate location of lightning as imaged by LOFAR is indicated by black (sparkles) and dark blue (other VHF sources) contours. The location of sparkles follow from the sparkle classification algorithm as described in Appendix B. A brief description follows of the five convective systems. It is the purpose of this section to provide a basic overview of the relevant storm dynamics.

Convective system A: Supercell

The radar images after 18:45 indicate that convective system A is a supercell. These systesm are characterized by a single, very strong updraft, mesoscale rotation in the updraft, and overshooting cloud tops (Markowski and Richardson, 2011). They typically produce much precipitation, large hail and much lightning (Markowski and Richardson, 2011; Calhoun et al., 2013). The reflectivity images in Fig. 3 show that system A persists as an isolated cell with heavy precipitation for more than two hours. On close inspection, a Bounded Weak Echo Region (BWER) (Lakshmanan and Witt, 1996; Markowski and Richardson,

https://doi.org/10.5194/egusphere-2025-6253
Preprint. Discussion started: 19 January 2026

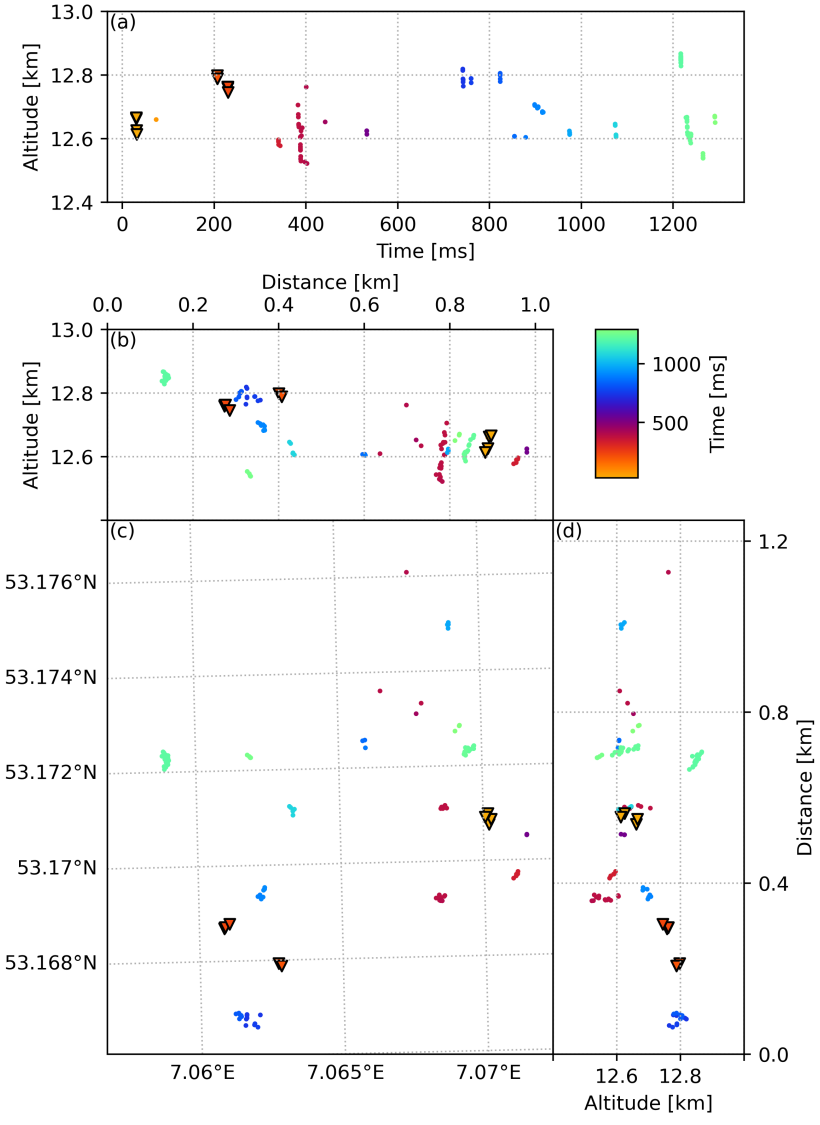

Figure 2. A zoom-in of the LOFAR image in Fig. 1. Triangles with black contours are the VHF sources marked as sparkles by the sparkle classification algorithm as described in Sec. 2.2.

https://doi.org/10.5194/egusphere-2025-6253
Preprint. Discussion started: 19 January 2026

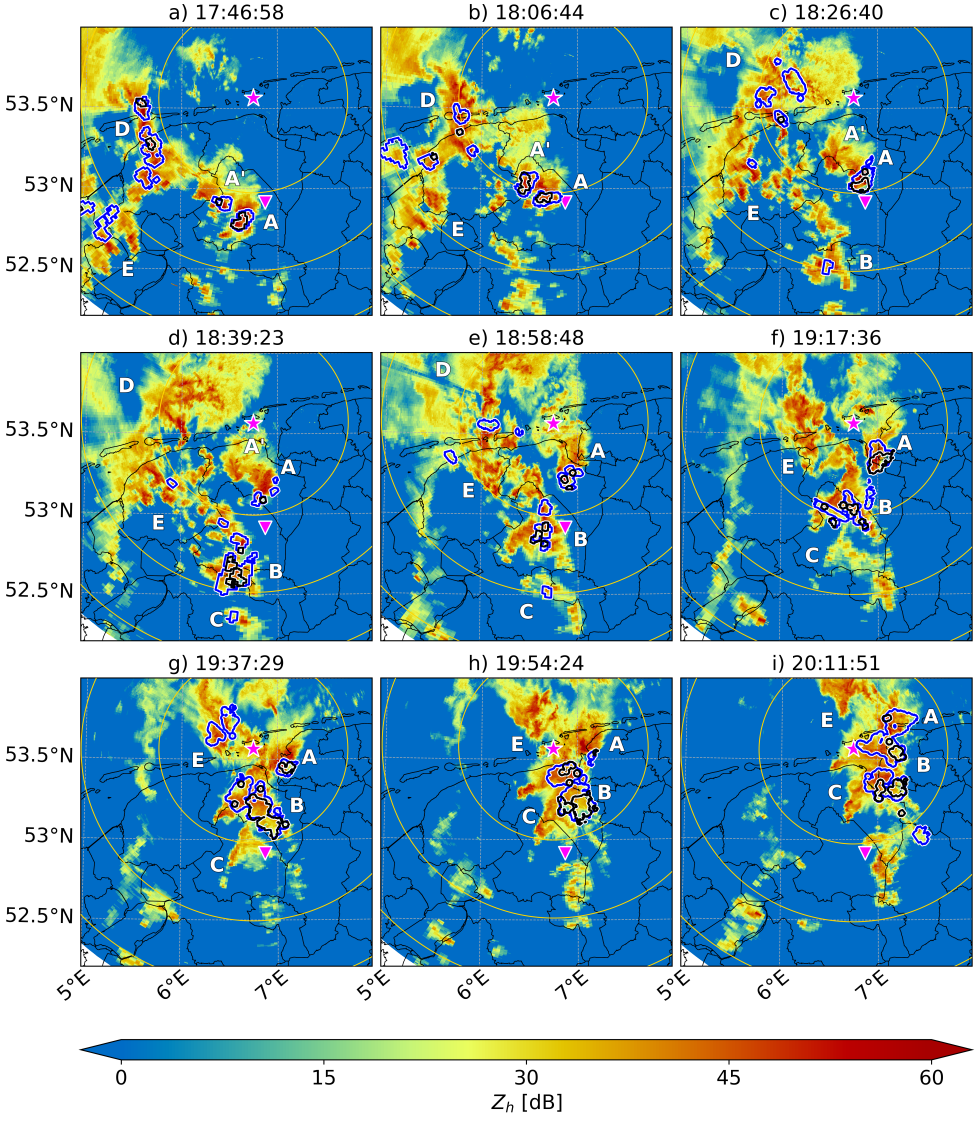

Figure 3. Radar reflectivity scans (1.5° elevation angle) of the storm at the time of the nine different LOFAR images. The black and dark blue contours mark the radar data within a 2 km horizontal distance of sparkles and other VHF sources, respectively. The annotations A-E indicate different convective systems as referred to in Sect. 3.2. The location of the radar and the LOFAR core are indicated by a pink star and triangle respectively. The (partial) rings centered around the radar indicate the altitude of the radar beam at 2, 4 and 6 km.

https://doi.org/10.5194/egusphere-2025-6253
Preprint. Discussion started: 19 January 2026

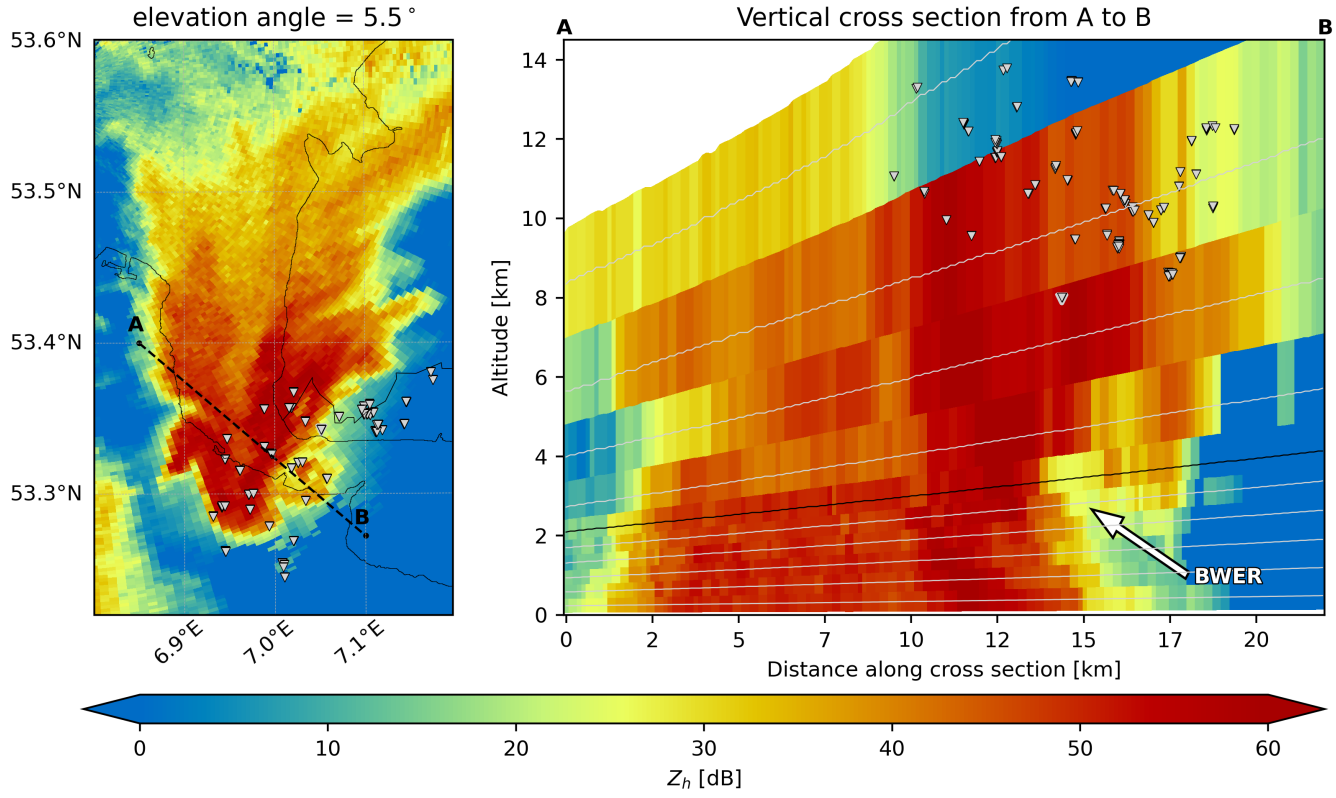

Figure 4. Radar reflectivity (Z_h) at 19:17:36 UTC with sparkles superimposed. Panel (a) shows a top view of the 5.5° elevation scan with sparkles projected onto the horizontal plane. Panel (b) shows a vertical cross section along the A–B line in panel (a), with sparkles within 10 km projected onto this plane. Radar beams from multiple elevation angles are indicated by gray lines, and the 5.5° beam from panel (a) is highlighted in black. The vertical extent of radar data in panel (b) does not reflect the actual 1° beam width. The Bounded Weak Echo Region (BWER) is annotated.

2011) is apparent. A BWER is a local zone of low reflectivity enclosed by higher reflectivity and is associated with the the strong updraft in a supercell (Musil et al., 1986). The BWER is annotated in Fig. 4, presenting both the top view and a vertical cross section.

Around 17:20 (not shown), system A splits into two distinct cells, A and A'. The two cells stay close together and are clearly distinguishable in Fig. 3a and 3b. At 17:46:58 (Fig. 3a) and 18:06:44 (Fig. 3b), both cells exhibit lighting, including sparkles. After 18:20, the intensity of A' decays (Fig. 3c-e) and it does not show any lighting in the LOFAR images. This decay happens after another split of cell A around 18:05 (barely visible in Fig. 3).

https://doi.org/10.5194/egusphere-2025-6253
Preprint. Discussion started: 19 January 2026

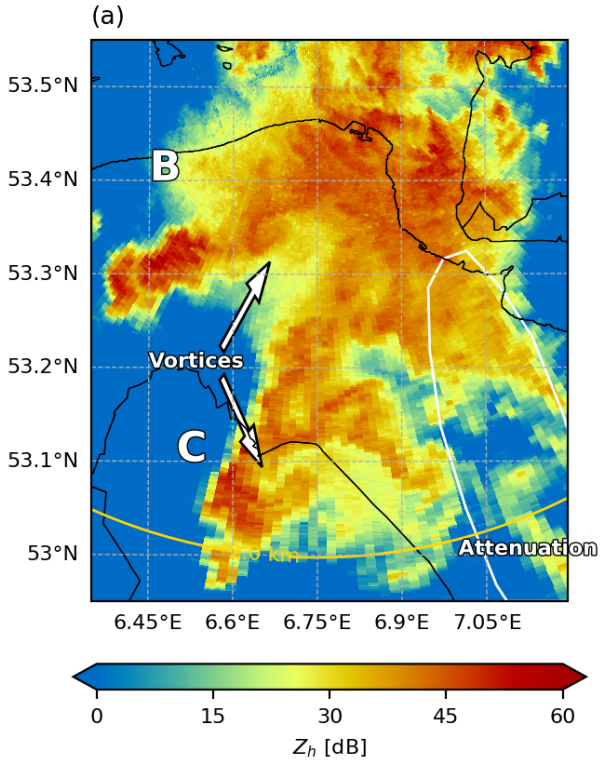

Figure 5. Top view of Z_h of convective system B (upper part) and C (lower part), at 19:54:24 UTC. Two large scale vortices are indicated by the arrows and a region expected to be subject to much attenuation is indicated by the white contour.

Convective system B

Convective system B appears relatively disorganized on the Borkum radar reflectivity scans. Around 18:20 (not shown), the system organizes itself into a larger, elongated structure. LOFAR images lightning for this system in every image from 18:26:40 onward. Sparkles are found at 18:39:23, 18:58:48, 19:37:29, 19:54:24, and 20:11:51. The image of 20:11:51 only contains a few sparkles.

Reflectivity images of systems B and C show vortices that are reminiscent of so called Bow Echos (Weisman, 2001). These type of radar images are associated with an intense kind of mesoscale convective system called squall lines (Markowski and Richardson, 2011). The typical bow shape with large scale vortices is illustrated in Fig. 5.

Convective system C

System C enters the range of the Borkum radar around 18:40. Before that time, it has been active as an isolated convective cell. After 18:40, the convective system starts to grow, and organizes into an arrow shape while catching up with system B. There seems to be interaction between system B and C, and around 19:15 the two systems connect in the radar images. The reflectivity

https://doi.org/10.5194/egusphere-2025-6253
Preprint. Discussion started: 19 January 2026

images show a narrow arm extending to the southeast from system C. At 18:39:23, 18:58:48, 19:54:24, and 20:11:51, LOFAR images show lightning in convective system C.

At 19:54:24 and possibly at 19:37:29, LOFAR images show sparkles where the anvil cloud of system C could interact with the anvil cloud of system B. In Fig. 3, the location of the heavy precipitation (high Z_h) does not match well with these sparkles. At higher altitudes, the sparkles do match the location of the highly reflective cloud much better. Therefore, we suspect that for this location, the signal in Fig. 10, is attenuated by the large amount of precipitation in the line of the radar beam. The white ellipse in Fig. 3 marks the area where we expect relatively much effect of attenuation.

Convective system D

Before 15:00, convective system D emerges at the Dutch west coast. Radar reflectivity values show that the system evolves between a state of multiple separated cells, and a north-south oriented line. The latter is for example observed in Fig. 3a. LOFAR images show lightning for system D at 17:46:58, 18:06:44 and 18:26:40. There are only a few VHF sources that are selected by the sparkle classification algorithm.

Convective system E

Around 16:00, south of system D, a convective system emerges that is annotated as E in Fig. 3. Between 17:20 and 18:00, system D, E, and a bow-shaped system seem to interact and form one larger system. This bow-shaped system (not visible in Fig. 3 resulted from a split of system A around 16:30.

From about 18:00 to 18:40, isolated convective cells emerge seemingly spontaneously between the system A, B and C. Since these cell later interact and merge, we also count these individual cells to system E. Eventually, system E moves over the Wadden Sea and it seems to organize into a large single system. LOFAR images show lightning for convective system E at 18:06, 18:26, 18:39, 18:58, and 19:37. The observed lighting is not considered to be sparkle activity.

3.2.1 Mesoscale interpretation

The naming of convective system A-E is inherently subjective, but it does provide a useful framework to distinguish between the lighting characteristics of seemingly separate convective events. We recognize that B, C and the individual convective cells grouped into system E (Fig. 3b-e) were initiated at approximately the same time along a line (approximately North-South oriented). This suggests that this convection was triggered by line of convergence (upward motion on the ground). Cell A appears to have initiated ahead of that line of convergence, but gets gradually overtaken. From 17:20 to about 18:10, system D aligns with this hypothetical line of convergence.

https://doi.org/10.5194/egusphere-2025-6253
Preprint. Discussion started: 19 January 2026

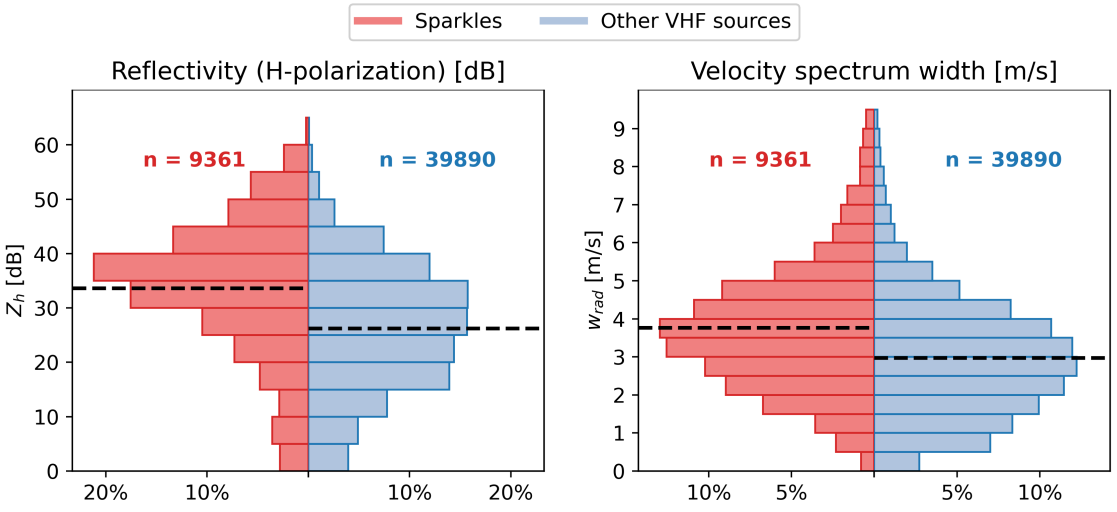

Figure 6. Histograms of radar reflectivity Z_h and radial velocity spectrum width W_r near sparkles compared to radar data near other VHF sources, according to the selection procedure described in Sect. 2.3. The dashed lines represent averages and the number of radar data points are indicated by the number n.

3.3 Quantitative analysis

Figure 6 shows histograms comparing the Z_h radar data near sparkles to radar data near other VHF sources. The distribution of sparkles shows a heavier tail for higher values for both Z_h and W_r. The dashed lines show that the average Z_h and W_r values are higher for sparkles than for other VHF sources.

Figure 7 shows 2-dimensional histograms of Z_h versus W_r in order to investigate correlations. Only when the counts in the histogram are normalized per Z_h bin (panels d and e), we see that there is a correlation between Z_h and W_r for both sparkles and other VHF sources. Namely, when the Z_h distribution is regarded as a prior, Fig. 7 suggests a convex shape in the W_r probability with respect to Z_h for both sparkles and other VHF sources. When we subtract the normalized 2-dimensional histograms of the two sets of data, we see in panel f that the probability of high W_r values holds for all Z_h values. However, the higher W_r probability is most pronounced for both the lowest $Z_h < 10$ bins. Reviewing the upper panel in Fig. 7, where the counts are not normalized per Z_h bin, the convex shape of the lower panels are hardly visible. This is because the counts in the $10 < Z_h < 45$ dB region are much more plentiful. This also underlines that the statistical significance of the W_r probability distributions at $Z_h < 10$ dB and $Z_h > 45dB$ are much lower.

Figure 8 shows the results of the HMC algorithm. For sparkles (red), a relatively larger percentage of radar data is classified as graupel/hail (RH). Near other VHF sources (blue), more data classified as ice crystals or dry snow. Figures 8b and 8c can be used to estimate the quality of the HMC algorithm. The performance of the HMC algorithm for each category can be estimated both with the maximum mean probability for each row, always found on the diagonal, and with the difference between the

https://doi.org/10.5194/egusphere-2025-6253
Preprint. Discussion started: 19 January 2026

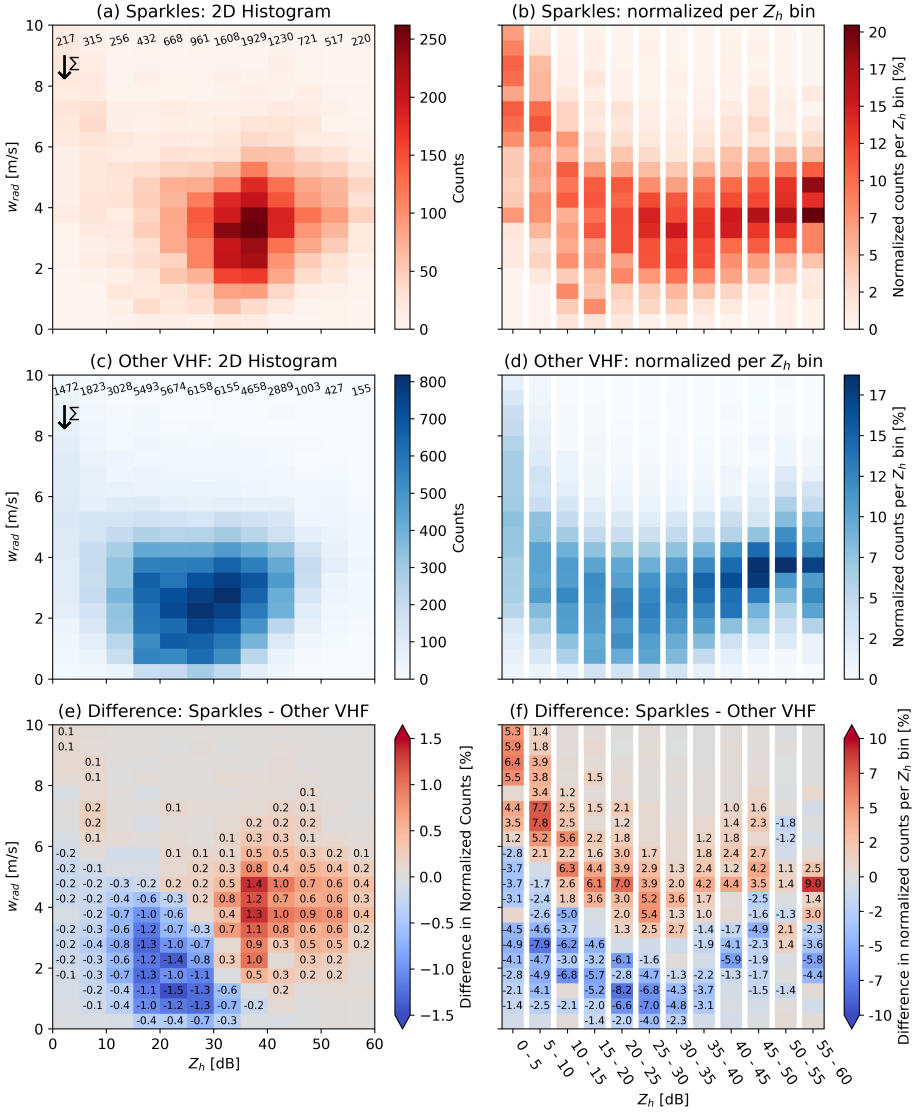

Figure 7. 2-dimensional histograms of the radar data near sparkles (a and b), the radar near other VHF sources (c and d), and the differences thereof (e and f). The histograms in panel (b) and (d) are normalized per Z_h-column. Panel (a) and (c) are counts per Z_h-W_r-bin. The number of counts per Z_h-column are annotated on top. In panel (b) and (d), the histograms are normalized with the number of counts in each Z_h-column. Panel (e) shows the difference between the normalized versions of (a) and (c). Panel (f) shows the difference between panel (c) and (d). The annotations of (e) and (f) correspond to the values and corresponding shading.

https://doi.org/10.5194/egusphere-2025-6253
Preprint. Discussion started: 19 January 2026

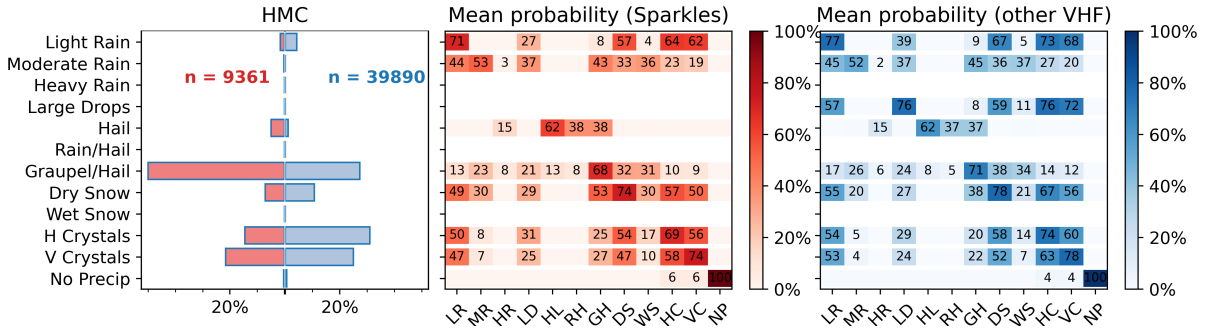

Figure 8. Panel (a) shows a histogram of the hydrometeor classification (HMC) algorithm for radar data near sparkles (red) and other VHF sources (blue). The number of included radar data points is indicated by the number n. Panel (b) and (c) show the probabilities for different hydrometeor types from the HMC algorithm, averaged over the data points in each bar of panel (a).

probabilities on each row. A larger difference between the maximum and other probabilities, indicates a better classification. The results show that the the "Graupel/Hail" and "Hail" classification are relatively certain, with a difference of ∼0.3 between the maximum and second highest mean probability. In contrast, the HMC algorithm has much more difficulty in distinguishing between "Dry Snow", "Horizontal Ice Crystals", "Vertical Ice Crystals" and "Light Rain" categories. These categories have a difference of ∼0.1 between the maximum and second highest mean probability. Regarding the orientation of ice crystals, we see relatively more vertical aligned ice crystals (VC) for sparkles. The opposite holds for other VHF sources.

3.4 Qualitative analysis

In order to understand the quantitative results in Sect. 3.3, we have also inspected the individual radar images. Figures 9, 10 and 11 show radar images with an overlay of contours to mark data corresponding to "sparkles" and "other VHF" sources. Note the threshold of 8 km altitude and the 0 dB reflectivity that is used to select radar data. Figures for additional radar elevation angles, for system A and B at times corresponding to LOFAR observations can be found in Appendix D.

A first observation is that the radar data near sparkles is always a subset of the radar data near other VHF sources. Although it is possible that large lightning structures exist in the same volume as sparkles, it is also possible that this is an effect of an incomplete sparkle classification algorithm. As mentioned in Sect. 2.3, incomplete sparkle clustering should have marginal effects on the statistics presented in section 3.3, because the subset of radar data near "sparkles" is excluded from the radar data near "other VHF" sources.

In general, the radar images often show high W_{rad} values where the radar beam exits a precipitation cloud at high altitudes. These areas often have low Z_h values and they likely mark the interface between the stratosphere and precipitation cloud. The cloud-stratosphere interface with low Z_h and high W_{rad} values are seen in the leftmost columns of Fig. 7e and 7f.

As expected from the histograms in Fig. 6, we see that the sparkles are often found in areas with high reflectivity values. We also note that within the sparkles data (black dotted contour), the radial velocity V_{rad} shows much divergence and rotation. This

https://doi.org/10.5194/egusphere-2025-6253
Preprint. Discussion started: 19 January 2026

is seen in the images as the radial and cross-radial gradients in the V_{rad} values respectively. The images show that locations with rotation and divergence are often accompanied by local points of relatively high W_{rad} values.

In Fig. 10 and Fig. 11 we observe that sparkles mainly surround the location of an intense, isolated updraft column. The approximate location of the updraft column at ∼10 km is indicated by a white ellipse. The main updraft location is revealed by the small patch of positive V_{rad} values. We interpret this isolated patch of positive V_{rad} as a combination of mesoscale rotation, and the updraft velocity that compensate for the downward sedimentation velocity of the hydrometeors. The intensity of the updraft, in terms of upward velocity, is highlighted by the observation that the Z_h values, and thus the sedimentation velocities, are high. We also note the relatively high W_{rad} values around the updraft column.

The location of the Z_h core in Fig. 11 is displaced $\sim 0.05°$ from the location of the updraft at ∼10 km (white ellipse). However, this displacement is roughly the same throughout the whole convective system. Therefore the displacement is probably related to advection between the different radar scans and the slanted orientation of the updraft columns. In Fig. 11, aliasing of the V_{rad} signal gives ambiguous rotation and divergence in the updraft column. However, we do clearly see local points of enhanced W_{rad} values for the patch of sparkle data.

For Fig. 9, one can use similar observations of positive V_{rad} patches where Z_h values are high to find two or three updraft columns. However, these locations are not so isolated as the updraft seen in Fig. 10. The locations are not indicated.

In accordance with the statistics in Fig. 8, the radar images show that locations of sparkles are correlated in regions that have been classified as graupel or hail (GH). Especially at high altitudes, for example in Fig. 11, we see that the sparkles data is more limited to areas that have been classified to feature graupel or hail (GH), whereas the other VHF data encompasses vast areas that have been classified to feature ice clouds (HC and VC).

4 Discussion

4.1 Sparkle classification

Given the clustering parameters as presented in Sect. 2.2, the sparkle classification algorithm yields satisfactory results. Given the proximity in space, we acknowledge that some small clusters (e.g. Fig. 2) and some isolated VHF sources may be misclassified as other VHF sources. We expect that the impact of such false negatives is marginal. Considering the 2 km radius to select radar data, many of the false negatives would be masked by the proximity of sparkles. We also note that changing the algorithm to reduce false negatives, for example by increasing the minimum number of VHF sources for a large cluster or by omitting the second stage of small-scale clustering, leads to more false positives. This is unfavorable for the selection of radar data, because the 2 km radius near sparkles gets priority over the 2 km radius near other VHF sources.

Scholten et al. (2023) show that some small-scale discharges are similar to so called “needles” discharges, and are related to positive-leader breakdown. Our two-stage clustering (first stage temporal margin $t = 0.3\,\mathrm{s}$) will likely merge such rapid, localized needle pulses, and any accompanying dart leaders, into larger clusters. Consequently, our results only represent sparkles that are not clearly linked to positive-leader breakdown.

https://doi.org/10.5194/egusphere-2025-6253
Preprint. Discussion started: 19 January 2026

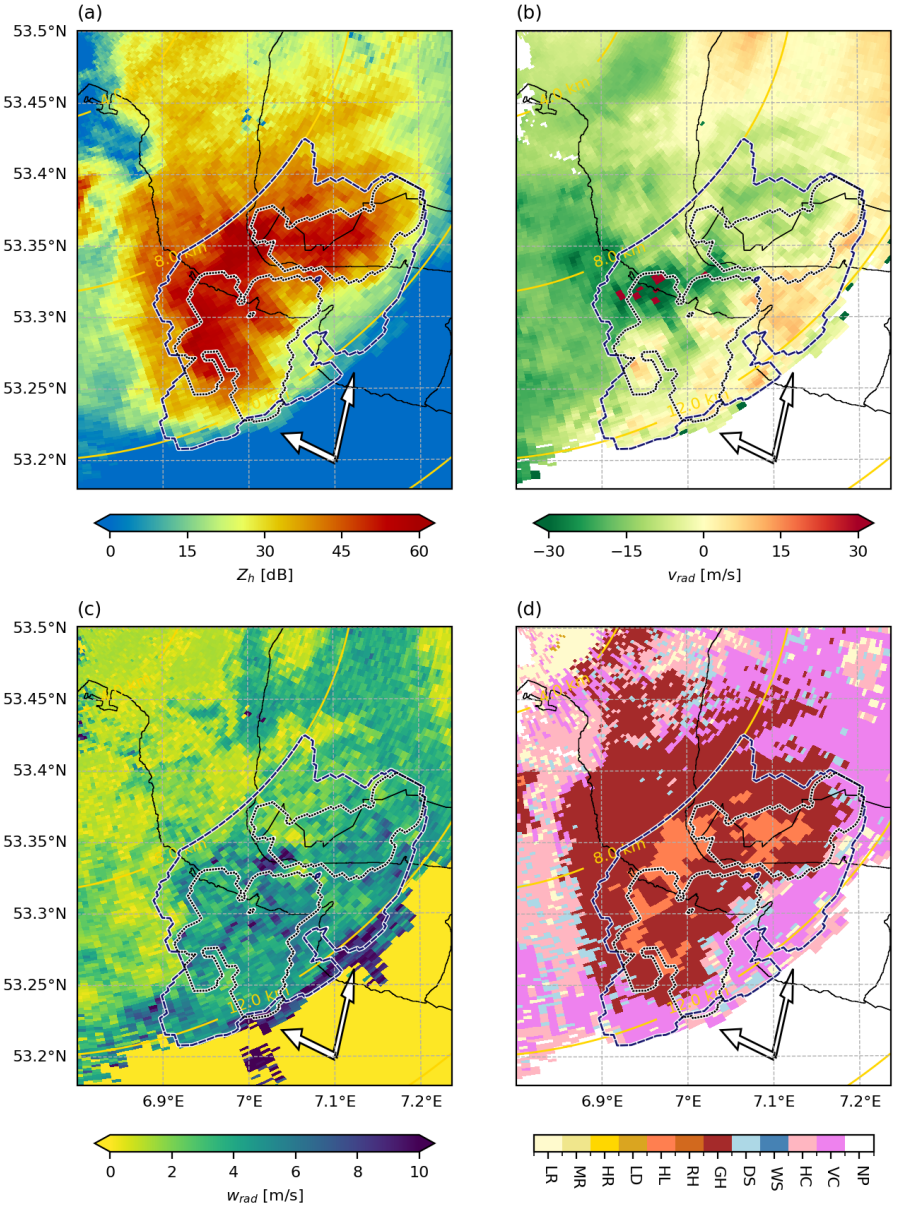

Figure 9. Top view of radar images at an elevation angle of 17°, around convective system A, at the time of the LOFAR image at 19:17:37 UTC with: (a) reflectivity Z_h, (b) radial velocity V_{rad}, (c) radial velocity spectrum width W_{rad}, (d) the Hydrometeor Classification Algorithm HMC. The radar resolution volumes within 2 km of sparkles (black dotted) and other VHF sources (blue dashed) are indicated by contours. Arrows indicate cloud edges with high W_{rad} values. Yellow arcs indicate the 8 and 12 km altitude of the radar data.

https://doi.org/10.5194/egusphere-2025-6253
Preprint. Discussion started: 19 January 2026

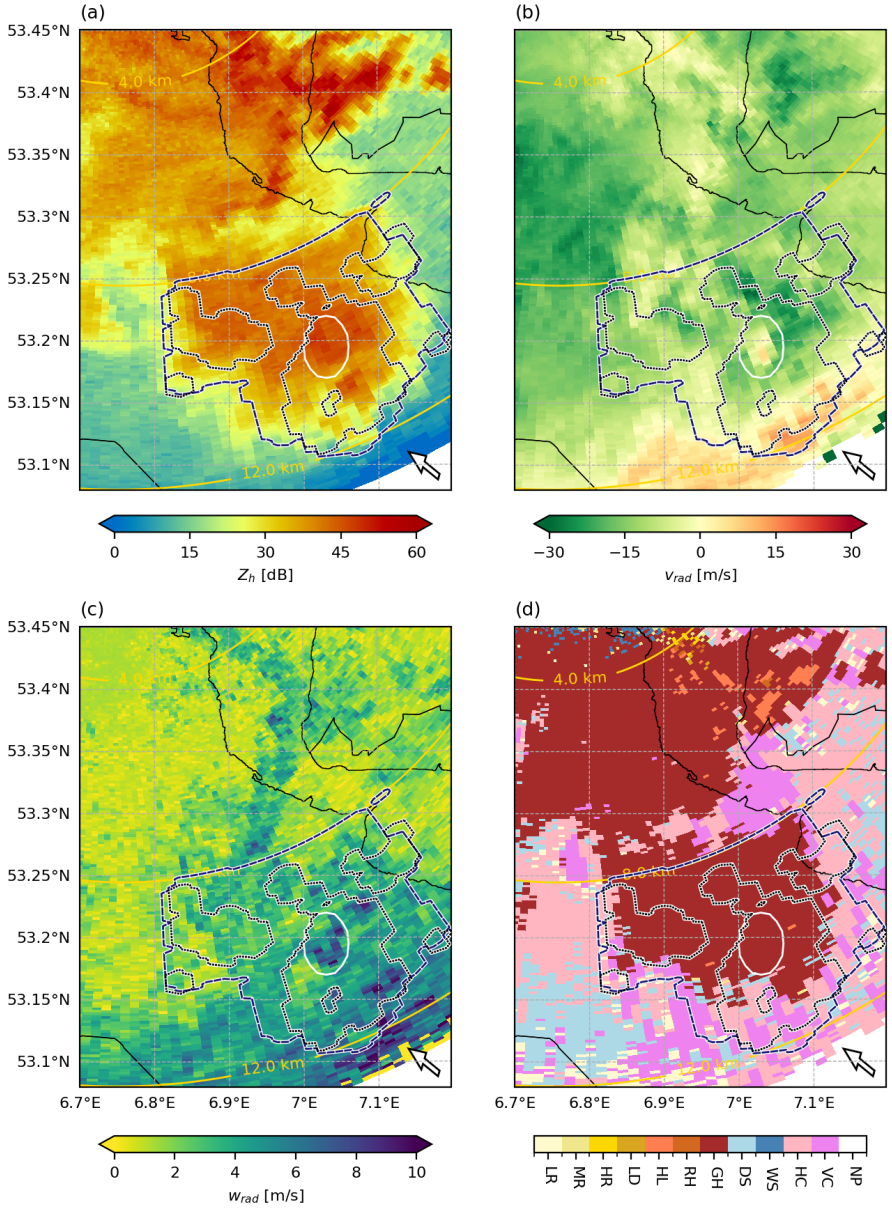

Figure 10. Similar to Fig. 9, but corresponding to the LOFAR image at 19:54:24, and at an elevation angle of 12°, focusing on system B. The white circle indicates an updraft column. Arrows indicate cloud edges with high W_{rad} values. Yellow arcs indicate the 4, 8 and 12 km altitude of the radar data.

https://doi.org/10.5194/egusphere-2025-6253
Preprint. Discussion started: 19 January 2026

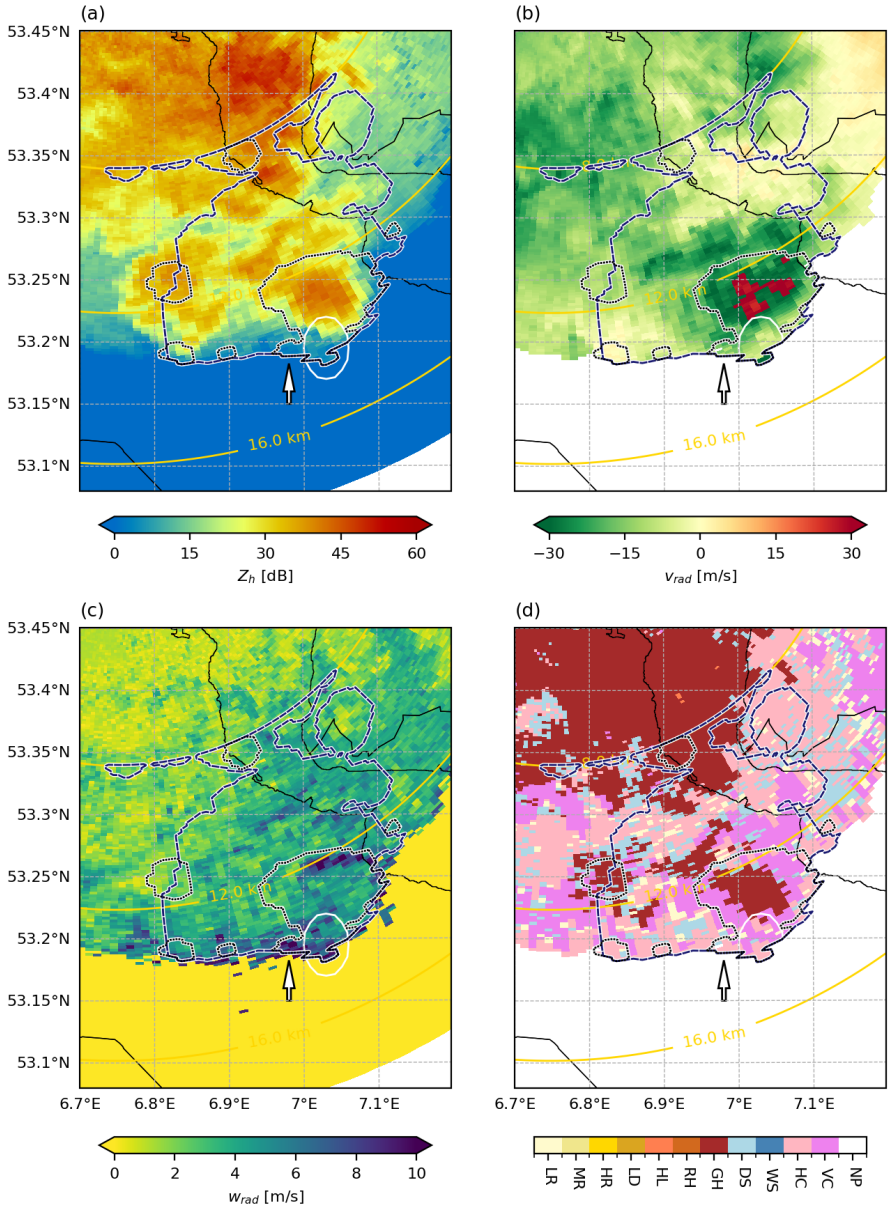

Figure 11. Similar to Fig. 10, but at an elevation angle of 17°. The white circle corresponds to the location of the white circle in Fig. 10. Arrows indicate cloud edges with high W_{rad} values. Yellow arcs indicate the 8, 12, and 16 km altitude of the radar data.

https://doi.org/10.5194/egusphere-2025-6253
Preprint. Discussion started: 19 January 2026

4.2 HMC algorithm

Although the classification for graupel/hail (GH) is relatively certain, panel b and c in Fig. 8 show that the distinction between horizontal crystals, vertical crystals, dry snow, and light rain is more uncertain. Therefore, we can not draw substantiated conclusions about any electric field effects on ice crystal alignment. On the other hand, we are confident that the surroundings of other VHF sources are often filled with ice crystals. For sparkles, the surroundings are dominantly filled with graupel/hail, but almost equally much space with ice crystals. That is, if we aggregate the horizontal and vertical ice crystals into one hydrometeor category.

Another aspect to consider for the fuzzy-logic algorithm is that it was originally designed for S-band radars. Because of their larger wavelength, S-band radars are less prone to Mie scattering and attenuation(Straka et al., 2000). Although previous work (Marzano et al., 2006; Overeem et al., 2020; Vulpiani et al., 2012a) has shown the potential of fuzzy-logic algorithms for C-band radars, attenuation and Mie scattering remain a source of error. The algorithm we use in this paper does compensate for Mie scattering, but no attempt is made to compensate for attenuation. For improved results, one may attempt a more complicated scheme to weight the different polarimetric variables, following Dolan et al. (2013).

4.3 Physical interpretation

Placing our results in the context of previous work, the following similarities are found. The correlation between high reflectivity values and sparkle-like lightning is also found by Emersic et al. (2011), Calhoun et al. (2013) and MacGorman et al. (2017). These studies also observe that these discharges form a cap on top of a very strong, vertical updraft, reaching high altitudes. Our study also suggests that sparkles are found at the top or above strong updrafts, based on three arguments. Firstly, the high reflectivity values at sparkle altitudes can logically only be present in or near updrafts. The large hydrometeors responsible for such high reflectivity values would quickly sediment down to lower altitudes were it not for the presence of strong updrafts. Secondly, the V_{rad} radar images indicate updrafts. For both system A and B, the images (see Appendix D) at low elevation angles show mesoscale rotation, indicated by cross-radial V_{rad} gradients, at locations with high Z_h values. For the radar image in Fig. 10, we even see a patch of positive V_{rad} values at about 10 km altitude, well above the low-level rotation. This indicates that the updraft extends up to more than 10 km altitude. Figure 11 shows the location of sparkles, just above this location. Thirdly, the relative location of the BWER and hook echo in system A indicate that the main updraft is much aligned with sparkles, especially when one considers that the updraft is likely to be slanted by wind shear. Unfortunately, time differences up to 2.5 minutes between radar and LOFAR data, broadening of the beam width, and the few radar elevation angles reaching sparkle altitudes (see Appendix A) inhibits the quantification of the distance between sparkles, updrafts, and cloud tops.

All of the aforementioned studies also specifically associate the sparkle-like discharges with the intensification of updrafts. The $\sim$20 minutes gap between LOFAR images complicates a detailed temporal analysis of sparkles. However, if the convective systems that produce sparkles are indeed a supercell and a squall line, it may be expected that updrafts were intense. The story line of the mesoscale events in convective system A, such as the development of a BWER and hook echo, would suggest intensifying updrafts around the time of sparkles. For convective system B, there are few mesoscale features that indicate the

https://doi.org/10.5194/egusphere-2025-6253
Preprint. Discussion started: 19 January 2026

updraft intensification matching the presence of sparkles. However, we think that attenuation obscured some of the dynamical features of the right-hand-side of system B (see Fig. 5), which produced many sparkles.

We are confident that for high Z_h values, the higher W_{rad} values near sparkles are mainly reflecting the enhanced atmospheric turbulence near sparkles. Turbulence enhances W_{rad} through wind-shear within the radar resolution volume (sub-resolution). Not only does wind shear drive turbulence, but the chaotic fluctuations of wind shear also constitute turbulence. Qualitative comparison shows that, for higher reflectivity values, enhanced W_{rad} values are generally accompanied by wind shear between radar resolution volumes. Thus, the driver for sub-resolution turbulence in cloud tops is clearly visible. Examples can be seen in Fig. 9 and Fig. 10 as spatial gradients in the V_{rad} image, at locations where both Z_h and W_{rad} values are high.

For low reflectivity values, it is likely that side-lobe contamination plays a role in enhanced W_{rad} values. This effect is most pronounced if, the Z_h value for a specific radar resolution volume is not high, bu Z_h values are high in the surroundings. In this case, the radar beam's side-lobes, which also probe the volume outside the targeted resolution volume, contribute disproportionally to the total returned signal. Because a larger volume contributes to the total signal, measured wind shear, and thus W_{rad} values, can increase. Examples of locations that are likely to be the result of side-lobe contamination, are marked with the arrows in Figs. 9-11.

Side lobe contamination explains the high W_{rad} values observed in Fig. 7 for the lowest Z_h bins. From Fig. 7f, it appears that the side-lobe contamination is more prominent for sparkles. This can be expected because the sparkles are, more often than other VHF sources, concentrated near highly reflective updraft columns. It is near these updraft columns that the spatial Z_h gradients, and thus side-lobe contamination is largest.

Since side-lobe contamination is most significant for low Z_h values, we are confident that the observed W_{rad} enhancement actually represents atmospheric turbulence for $Z_h > 15$ dB.

Another mechanism that can increase W_{rad} values, is differential sedimentation of mixed hydrometeors. However, because the radar elevation angles are relatively low ($\leq 25°$), the sedimentation velocities, which are inherently vertical, are a minor contribution to the spectrum of the velocity in the direction of the radar beam. Additionally, this type of enhancement is most pronounced when the backscattered signal is not dominated by a single type of hydrometeor. The HMC algorithm shows, comparing the numbers between the rows in Fig 8, that the uncertainty in the classification is similar for both sparkles and other VHF sources. Therefore, we conclude that for sparkles, there is no increased hydrometeor mixing and thus no enhanced W_{rad} through differential sedimentation.

The presence of intense turbulence near sparkles, as suggested by the enhanced W_{rad} values, may be important for the relevant charging mechanisms that explain the presence of these small-scale lightning structures. Non-inductive charge separation is generally considered to dominate the charging mechanism in thunderclouds. However, the inductive charging might be considerable in certain conditions. Mareev and Dementyeva (2017) showed that for turbulent conditions, an ambient electric field and hydrometeors of adequate size, the inductive charging mechanism may lead to exponential growth of the electric field.

https://doi.org/10.5194/egusphere-2025-6253
Preprint. Discussion started: 19 January 2026

Supposing that the local spots of enhanced W_{rad} values represent the fine scale turbulence needed for significantly enhance the inductive charging mechanism, this could explain the intermittent behavior of sparkles that is observed by LOFAR.

As suggested by Calhoun et al. (2013), the proximity of the charged screening layer and the lofted charge in the updraft might enhance the electric field at the top of the updraft. For sparkles, the higher reflectivity values and graupel/hail classification indeed suggest that the lofted charge, carried by large hydrometeors, is brought closer to the stratosphere where the charged screening would be most pronounced.

In light of the small spatial extent of sparkles, we evaluate mechanisms that could form charge pockets and thereby limit growth of sparkles. Modeling work by Calhoun et al. (2014) shows that charge pockets may be related to heterogeneous charging in the updraft column. Turbulence in cloud tops could fragment those pockets down to the ~ 100 m length scale associated with sparkles. Our results do not clarify the role of heterogeneous updraft charging. However, given our observation of increased turbulence near sparkles, turbulent fragmentation seems plausible. Alternatively, MacGorman et al. (2017) suggest that velocity gradients at the top of overshooting clouds may cause folding of a charged screening layer into the cloud. The folding process could potentially form pockets of the oppositely charged screening layer wrapped into the cloud. If so, we would expect to see a complex V_{rad} pattern along the top-edge of the cloud. In Fig. 10b, near sparkles (black dotted contour), we indeed see a "frayed" pattern in the V_{rad} gradient at between 11 and 12 km altitude. Folding in cloud tops could also be related to the irregular coiled shapes in both the Z_h and V_{rad} images near sparkles. We also note that the mechanism to drive screening layer folding, namely wind shear, may be visible as enhanced W_{rad} values at the top-edge of clouds. For example near the 12 km contour line of Fig. 9. However, we cannot distinguish tropopause wind-shear from side-lobe contamination (arrows in Figs. 9-11).

Altogether, our observations are compatible with both hypotheses of (1) folding of a screening layer into the cloud, and (2) turbulent fragmentation of charge pockets. These mechanisms may act jointly.

4.4 Outlook

This study uses a unique combination of high resolution lightning data and operational weather data. Further research with similar methods may disclose the location of sparkles with respect to a charged screening layer, charge pockets, and enhanced turbulence.

A first improvement for future studies will come with the release of LOFAR 2.0, planned for 2027. The new system can observe significantly more flashes per storm. This will allow a better comparison of the temporal development of lightning and sparkles with the thunderstorm dynamics.

It would be most useful to deploy a mobile research radar for the study of sparkles. Using more steep elevation angles, potentially with an adaptive scanning strategy that focuses on the overshooting cloud tops, would allow to get a much higher vertical resolution in the location which is most relevant for sparkles. Additionally, an extended analysis of the radar data, for example, a spectral analysis similar to (Mak and Unal, 2025), could provide more information on the mixture of different hydrometeors and the source of the observed W_{rad} enhancement.

https://doi.org/10.5194/egusphere-2025-6253
Preprint. Discussion started: 19 January 2026

Finally, the instruments aboard the Meteosat Third Generation (MTG) satellite (Holmlund et al., 2021) that was launched in 2022 could provide useful information on the relation between cloud top height and lightning. In particular, matching the MTG lightning data with LOFAR lightning images may reveal whether the sparkles occur above the clouds.

5 Conclusions

In this study we have investigated the atmospheric conditions associated with the occurrence of small-scale intermittent lightning discharges at the top of thunderstorms, called "sparkles". To this extent, we have compared volumetric weather radar data with LOFAR high-resolution lightning images. Our results show that sparkles occur near high radar reflectivity values at high altitudes. Such values are associated with strong updrafts, lofting of graupel, and overshooting cloud tops. An algorithm for hydrometeor classification confirmed the dominance of graupel near sparkles. In the proximity of sparkles we also observe enhanced W_{rad} values and heterogeneous V_{rad} patterns. We are confident that this signal represents enhanced turbulence near sparkles. We hypothesize that the turbulence, through the creation of charge pockets, is crucial for the small spatial extent and intermittent behavior of sparkles. It is not evident if turbulence plays a role solely by mixing, or also through enhanced inductive charging.

The two convective systems that produced sparkles resembled a supercell and a bow echo. The latter is the first known case of a bow echo to produce sparkles or sparkle-like discharges. It remains unclear what this finding could indicate about the nature of sparkles.

Our findings may have a practical application for now-casting of severe weather. We show that the presence of sparkles reveals severe thunderstorms and the location of intense updrafts. Therefore, implementation of a sparkle detection algorithm on live high resolution lightning data, would provide a fast way to warn for meteorological hazards that accompany severe thunderstorms.

Although our results do not fully clarify the hypotheses about the physics of sparkles, our research does pave the way for further research. Our methods may serve as inspiration for future research comparing LOFAR lightning images with radar data. Furthermore, our conclusions could be used as a starting point for research with a more bottom-up approach to study atmospheric perquisites for, and the physical mechanisms of, sparkles. Such future research could consider our proposed hypotheses of turbulent enhancement of inductive charging.

. **Code and data availability:** The data that is used in this study (LOFAR and Borkum radar) is available on Zenodo (https://doi.org/10.5281/zenodo.17778 ERA5 reanalysiss volume data of the temperature, meridional wind, and zonal wind, can be downloaded in the Climate Data Store from the Copernicus Climate Change Service Hersbach et al. (2023). The python code to analyze the data and reproduce figures is available in a the github repository https://doi.org/10.5281/zenodo.1794899 (van Loon, 2025).

https://doi.org/10.5194/egusphere-2025-6253
Preprint. Discussion started: 19 January 2026

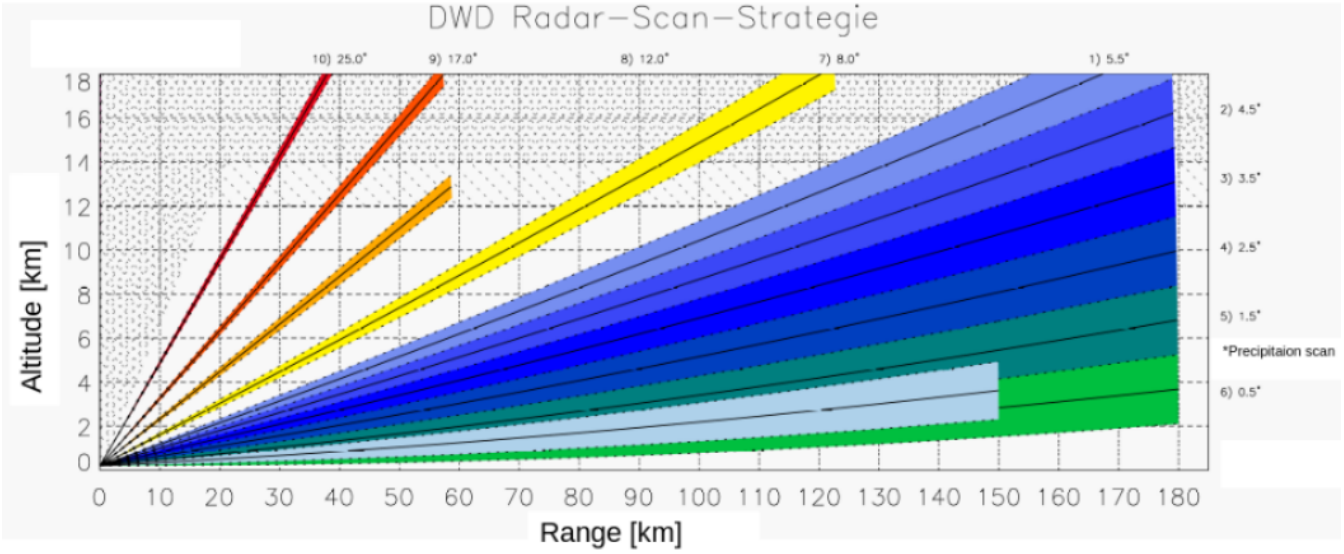

Figure A1. Adapted version of figure from Frech et al. (2017). Scanning strategy of the DWD radar on Borkum. Different radar beams and the 1° beam width are represented by shadings. The corresponding elevation angles are shown at the side of the axes. *The precipitation scan is not used in this study.

Appendix A: Radar data

A1 Borkum radar

The Borkum radar is a so called C-band radar with a frequency range of 5600-5650 MHz. It scans the atmosphere at 10 elevation angles between 0.5° and 25° with a beam width of 1°, and a range bin separation of 250 meter. Fig. A1 shows a diagram of the scanning strategy with the elevation angles. The volume scanning procedure is repeated every 5 minutes. The raw data was processed by the German Meteorologival service (Deutsches Wetterdienst). For detailed information about the radar and data, we refer the reader to Frech et al. (2017).

A2 Radar errors

The frequency of the polarimetric radar determines the sensitivity to different types of hydrometeors. C-band radars are most suitable for particles with a diameter between approximately 0.5 - 7 mm. Smaller particles hardly scatter the radar pulse and large particles may cause resonance effects. Resonance effect may cause very high Z_h values and spatial discontinuities in the scatter properties. This means that large hail stones, snow flakes or very large droplets may complicate the interpretation. In this study, corrections are made for resonance effects for the computation of the specific phase difference ϕ_{dp}. The ϕ_{dp} variable is used in the computation for HMC. The algorithm is described in Appendix B.

https://doi.org/10.5194/egusphere-2025-6253
Preprint. Discussion started: 19 January 2026

For C-band radars, attenuation of the radar can be considerable. The blockage of the radar beam by a highly reflective atmosphere will decrease the measuring skill behind. This may introduce a negative bias of Z_h. For V_{rad} and W_{rad}, attenuation increases the uncertainty. In this study, we do not attempt to computationally correct for attenuation.

Appendix B: Data processing

ERA5 data

We use the ERA5 reanalysis data(Hersbach et al., 2023) for the ambient temperature (in the HMC algorithm) and the horizontal wind velocity (advection of radar data). The ERA5 data is hourly and comes on fixed pressure levels. We used the geopotential to convert the ERA5 data to the height, and interpolate linearly in space and time to the radar data points.

B1 Geospatial data processing

There are two important factors to consider for a valid spatial analysis, the georeferencing of the radar data and the time difference between radar and LOFAR data.

For georeferencing the radar data, the `wradlib.georef.georeference` algorithm (Heistermann et al., 2013) has been applied. This algorithm makes uses of the equations provided (Doviak et al., 1993) that take into account the curvature of the earth and the refractive index of the atmosphere. A standard value of $k_e = 4/3$ is used as the refractive index compensation factor.

The native output of this ωradlib Python algorithm is in an azimuthal equidistant projection. For comparison, LOFAR data is converted to the same azimuthal equidistant projection. All figures that include radar data have the radar's native azimuthal equidistant projection.

In order to deal with the time difference Δt between LOFAR data and radar data, we apply advection to the radar data to match the time of LOFAR images. In this study, we perform no temporal interpolation of the radar data. Instead, we use the time of the LOFAR image of interest and we collect the radar scans at each elevation angle that are closest in time. Subsequently, we linearly interpolate the the horizontal wind velocities of the ERA5 data of June 18 2021 in time and space on to the location of each radar data point. This yields the horizontal wind vector $\boldsymbol{v}_i$, corresponding to each data point with index i. These values are used to move the georeference $\boldsymbol{x}_i$ of the each radar data point over a distance of $\Delta \boldsymbol{x}_i = \Delta t_i \cdot \boldsymbol{v}_i$. Here, Δt_i is the time difference between the LOFAR data and each radar data point.

In practice, the advection scheme moves the radar data up to 3 km. This is not surprising given the maximum time difference of 150 seconds for the 5 minute radar scanning procedure and the high altitude wind velocities of more than 30 m/s. Within one sweep there are sometimes be significant differences in advection shifts. Especially between the first and last scanning azimuth. Although the data is adjacent in space, a time difference of ~ 20 seconds gives a large jump in advection distance. Another large jump in advection distances is visible where the radar beam intercepts the tropopause. This is a result of significant wind gradients at this altitude.

https://doi.org/10.5194/egusphere-2025-6253
Preprint. Discussion started: 19 January 2026

To reduce computational cost, the ERA5 altitudes are replaced by the average altitude of each model level. As a results, the ERA5 data is structured on a Cartesian grid and the interpolation towards the radar data points is less costly.

B2 Matching radar and LOFAR data

The `scipy.spatial.KDTree.querry_ball_point` function is used for collecting the radar points within a radial distance of the LOFAR data. In all results, a radial distance of 2 km is used as a threshold for proximity. This is a subjective choice, that seems reasonable keeping in mind the poor vertical radar resolution up to 4 km, the temporal radar resolution of 5 minutes, and the uncertainties in advection over such timescales.

B3 Computing K_{dp}

In the radar data, we have the total differential phase ψ_{dp}. We use the ωradlib Python package (Heistermann et al., 2013) for filtering and computing the differential phase shift ϕ_{dp} and the specific differential phase K_{dp} values. The result is highly depend on filtering and correction choices, this subsection describes the specifics on the ψ_{dp} processing details.

In general ψ_{dp} is noisy. The general approach used to retrieve a more meaningful ϕ_{dp} and computing the K_{dp} signal follows the method as described by Vulpiani et al. (2012b). The described method is an iterative process based upon 4 four steps:

1. K_{dp} is calculated using a finite difference method on the ψ_{dp} signal: K'_{dp}
2. K_{dp} values are filtered for realistic values such that $\kappa_1 < K'_{dp} < \kappa_2$. When this condition is not met, K'_{dp} is replaced with a zero value. This method attempts to remove noise and backscatter phase δ_{hv}. Potential phase folding should be taken into account to prevent unnecessary data loss.
3. $\hat{\phi}_{dp}$ is reconstructed by integration of the filtered K'_{dp}.
4. K_{dp} is computed from $\hat{\phi}_{dp}$: $\hat{K}_{dp}$

It is important to realize that the computation of K_{dp} makes use of a smoothing window. This has a twofold purpose. Not only does it smooth the noisy ψ_{dp} signal, it also deals with values outside the $\kappa_1 - \kappa_2$ range. Once the $\kappa_1 < K'_{dp} < \kappa_2$ is not met, K'_{dp} values are replaced by zero's. These nonphysical zero values are compensated by smoothing of the neighbouring values. For this reason, Vulpiani et al. (2012b) suggests to iterate over steps 3 and 4.

Another important artifact to consider is that phase measurements are prone to phase folding. The phase measurements are limited to $180°$, such that when a phase shift is increased beyond $180°$, it jumps to $-180°$. The opposite holds for the phase decreasing from $-180°$, that results in a jump to $180°$. Phase jumps always lead to K'_{dp} values outside the $\kappa_1 - \kappa_2$ range and subsequently data loss. Therefore, it is useful to try to unfold the phase folds into a useful signal.

Although powerful because of the smoothing, and because of the independence of ψ_{dp} calibration offsets, the method by Vulpiani et al. (2012b) in the`wradlib.dp.phidp_kdp_vulpiani` function has a major shortcoming during phase unfolding. The unfolding is based on K'_{dp} computed with a central finite difference method. This method duplicates unwanted artifacts around the artifact itself. This may lead to unforeseen phase unfolding. Moreover, the suggested unfolding algorithm

https://doi.org/10.5194/egusphere-2025-6253
Preprint. Discussion started: 19 January 2026

only permits for a single, $180°$ addition, to correct for phase folding. Therefore, it cannot cope with multiple folds or a fold in the decreasing $-180°$ direction. In such cases, data is lost because of the $\kappa_1 < K'_{dp} < \kappa_2$ restriction on K_{dp} in step 2. Finally, the Vulpiani et al. (2012b) method does not include possibilities for noise masks. The iteration of smoothed k_{dp} does compensate somewhat for random noise. However, the correction for the phase fold takes place before the smoothing.

To increase the performance on phase folds, we applied the following algorithm for ψ_{dp} processing:

1. Changes in ψ_{dp} are neglected for low reflectivity values. E.g. where $Z_h < z'$ or $Z_v < z'$.
2. Phase unfolding by a modified `wradlib.dp._unfold_phidp_naive` Python function based on Wang and Chandrasekar (2009). This algorithm differentiates between noise and actual phase folds, by comparing ρ_{hv} and the preceding standard deviation. We modified the algorithm in order to tune the thresholds on the realistic propagation specific phase κ_1 and κ_2, the threshold for fold recognition K_{fold}, and the threshold for the maximum standard deviation σ_w.
3. K_{dp} values are filtered for realistic values such that $\kappa_1 < K'_{dp} < \kappa_2$. When this condition is not met, K'_{dp} is replaced with a zero value.
4. $\hat{\phi}_{dp}$ is reconstructed by integration of the filtered K'_{dp}.
5. K_{dp} is computed from $\hat{\phi}_{dp}$: $\hat{K}_{dp}$

For this study, the values for the filtering parameters in the above method are: $\kappa_1 = -5°$, $\kappa_2 = 20°$, $z' = 0$ dB, $\sigma_w = 0.8$. The size of the rolling window, for computation along the radar beam is 11 bins.

Appendix C: LOFAR

The following figures show LOFAR images with sparkle classification, zoomed-in on particular convective systems. They illustrate the nature of sparkles, as clouds of intermittent small-scale lighting discharges at high altitudes, and the performance of the sparkle classification algorithm. This is only a subset of all the LOFAR data used in this study.

Appendix D: Radar images

The figures in this appendix contain radar images of different radar variables of convective cell A and B, for times corresponding to LOFAR images.

. **Author contributions:** RVL conducted the main analysis and prepared the manuscript and figures. OS and BMH provided the LOFAR data and lightning expertise. HL assisted with radar-data interpretation. All authors, but especially JDA, contributed to the text revisions and data interpretation.

https://doi.org/10.5194/egusphere-2025-6253
Preprint. Discussion started: 19 January 2026

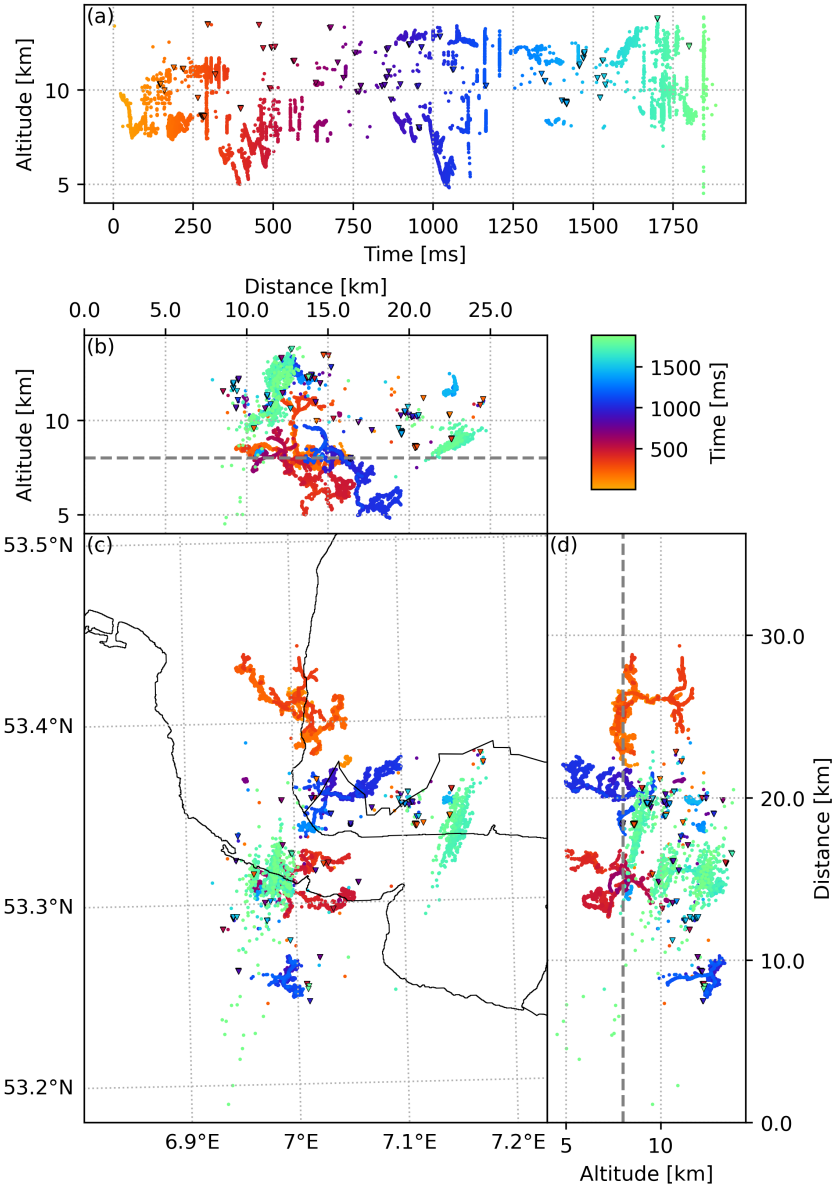

Figure C1. Similar to Fig. 2, but part of the LOFAR image at 19:17:36. The horizontal extent of panel (c) matches with Fig. 9. The gray dashed lines in panel (b) and (c) indicate the 8 km altitude threshold for sparkle selection.

. **Competing Interests:** We declare no competing interests.

. **Acknowledgments**

https://doi.org/10.5194/egusphere-2025-6253
Preprint. Discussion started: 19 January 2026

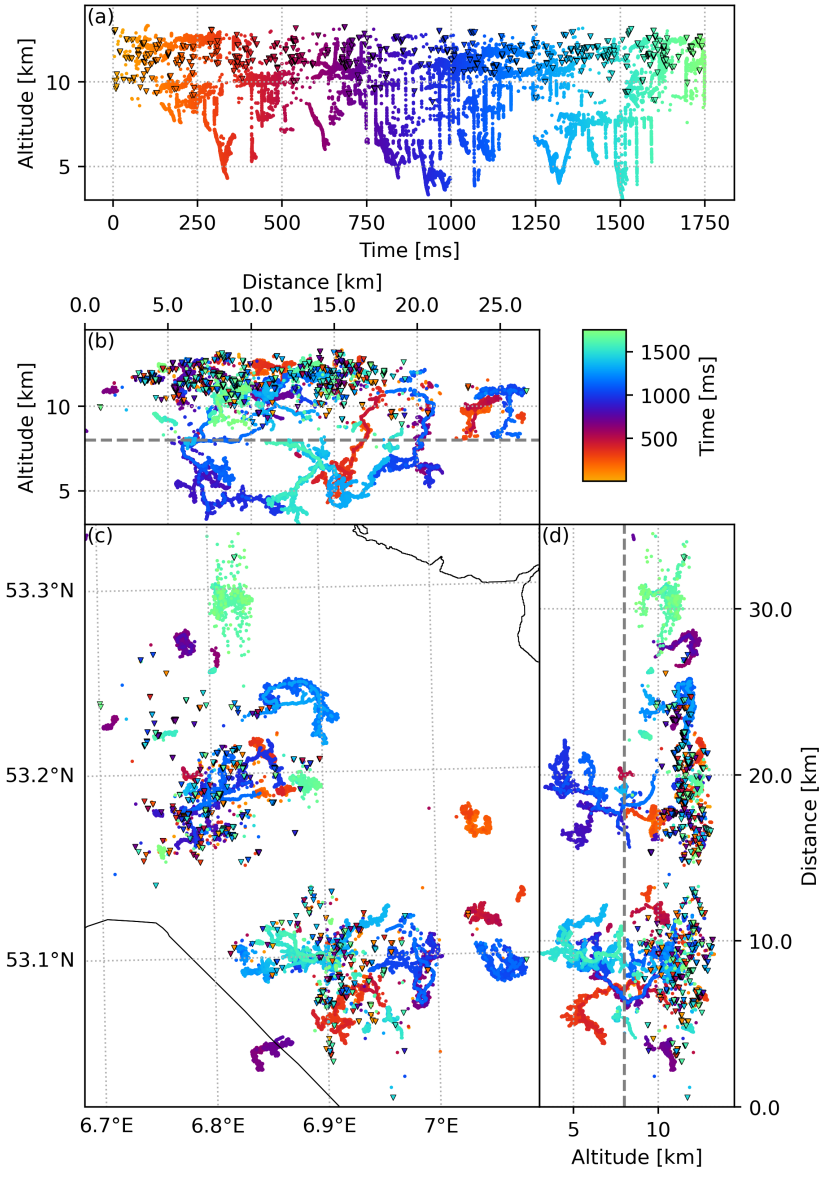

Figure C2. Similar to Fig. C1, but part of the LOFAR image at 19:37:29, and focusing of convective system B.

We thank the Deutsche Wetterdienst (DWD) for providing the data of the meteorological radar on Borkum Island in Germany for June 18, 2021. We also thank Jan Fokke Meirink for his help with satellite data during the initial, exploratory stage of this study. B. M. Hare is supported by ERC Grant Agreement No. 101041097.

This study is based on data obtained with the LOFAR telescope (LOFAR-ERIC). LOFAR (van Haarlem et al., 2013) is the Low Frequency Array designed and constructed by ASTRON. It has observing, data processing, and data storage facilities in several countries, that are

https://doi.org/10.5194/egusphere-2025-6253
Preprint. Discussion started: 19 January 2026

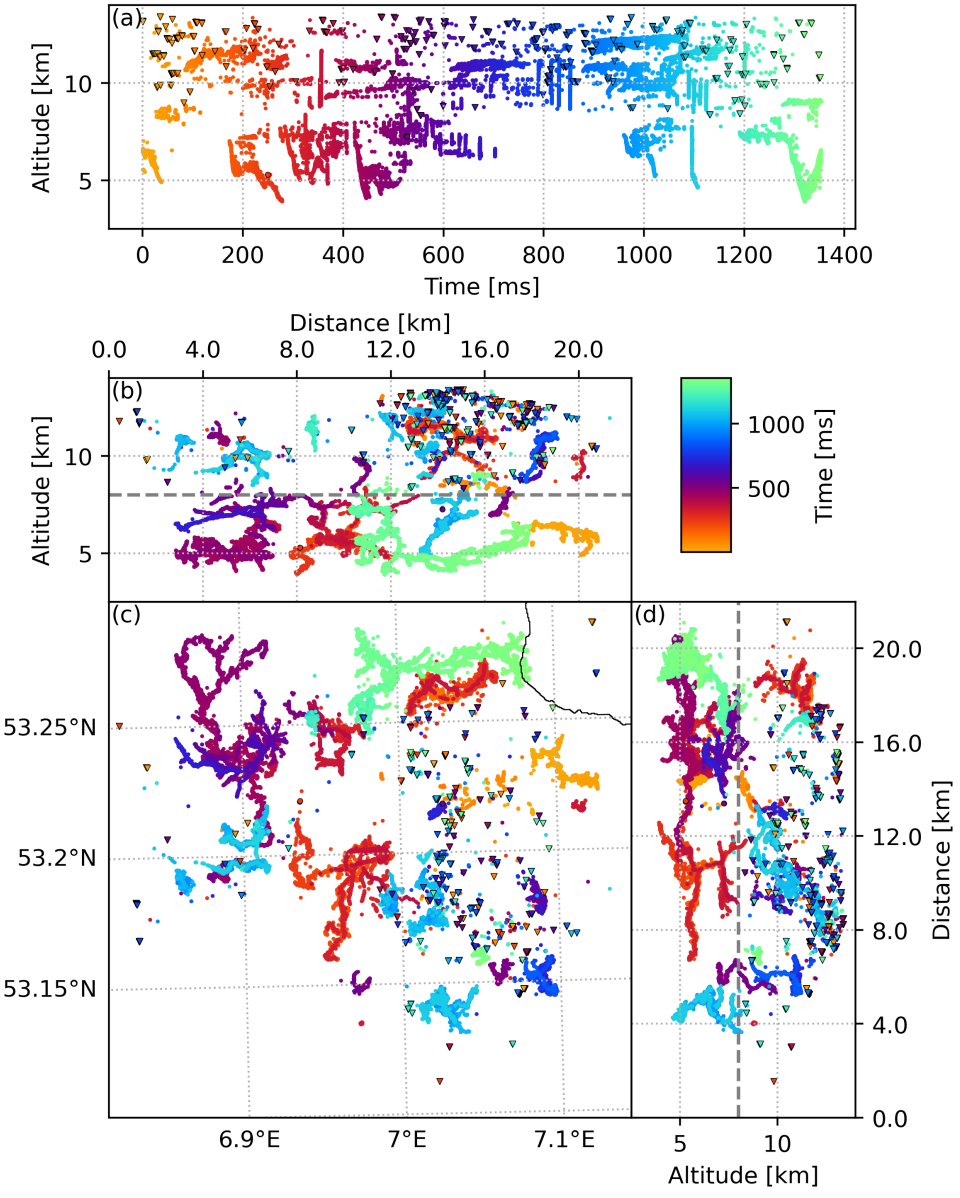

Figure C3. Similar to Fig. C1, but part of the LOFAR image at 19:19:54, and focusing on convective system B. The horizontal extent of panel (c) matches with Fig. 1. The VHF sources with a point shape and black contour are marked as sparkles by the two-stage clustering process, but fall below the 8 km altitude threshold.

owned by various parties (each with their own funding sources), and that are collectively operated by the LOFAR European Research Infrastructure Consortium (LOFAR-ERIC) under a joint scientific policy. The LOFAR-ERIC resources have benefited from the following recent major funding sources: CNRS-INSU, Observatoire de Paris and Université d'Orléans, France; Istituto Nazionale di Astrofisica (INAF),

https://doi.org/10.5194/egusphere-2025-6253
Preprint. Discussion started: 19 January 2026

Italy; BMBF, MIWF-NRW, MPG, Germany; Science Foundation Ireland (SFI), Department of Business, Enterprise and Innovation (DBEI), Ireland; NWO, The Netherlands; The Science and Technology Facilities Council, UK; Ministry of Science and Higher Education, Poland.

In the preparation of this manuscript, OpenAI's ChatGPT (version 4, 4o, and 5, from September 2023 to November 2025) was used to generate and improve python code, and to improve the text in terms of language style and fluency. All suggestions from generative AI were consciously considered. The authors take full responsibility of the text and code of this publication.

https://doi.org/10.5194/egusphere-2025-6253
Preprint. Discussion started: 19 January 2026

References

Al-Sakka, H., Boumahmoud, A.-A., Fradon, B., Frasier, S. J., and Tabary, P.: A new fuzzy logic hydrometeor classification scheme applied to the French X-, C-, and S-band polarimetric radars, Journal of Applied Meteorology and Climatology, 52, 2328–2344, 2013.

Calhoun, K. M., MacGorman, D. R., Ziegler, C. L., and Biggerstaff, M. I.: Evolution of lightning activity and storm charge relative to dual-Doppler analysis of a high-precipitation supercell storm, Monthly Weather Review, 141, 2199–2223, 2013.

Calhoun, K. M., Mansell, E. R., MacGorman, D. R., and Dowell, D. C.: Numerical simulations of lightning and storm charge of the 29–30 May 2004 Geary, Oklahoma, supercell thunderstorm using EnKF mobile radar data assimilation, Monthly Weather Review, 142, 3977–3997, 2014.

Dolan, B., Rutledge, S. A., Lim, S., Chandrasekar, V., and Thurai, M.: A robust C-band hydrometeor identification algorithm and application to a long-term polarimetric radar dataset, Journal of Applied Meteorology and Climatology, 52, 2162–2186, 2013.

Doviak, R. J. et al.: Doppler radar and weather observations, Elsevier Inc, Academic Press, 1993.

Emersic, C., Heinselman, P., MacGorman, D. R., and Bruning, E.: Lightning activity in a hail-producing storm observed with phased-array radar, Monthly Weather Review, 139, 1809–1825, 2011.

Frech, M., Hagen, M., and Mammen, T.: Monitoring the absolute calibration of a polarimetric weather radar, Journal of Atmospheric and Oceanic Technology, 34, 599–615, 2017.

Fuchs, B. R., Bruning, E. C., Rutledge, S. A., Carey, L. D., Krehbiel, P. R., and Rison, W.: Climatological analyses of LMA data with an open-source lightning flash-clustering algorithm, Journal of Geophysical Research: Atmospheres, 121, 8625–8648, 2016.

Hare, B., Scholten, O., Bonardi, A., Buitink, S., Corstanje, A., Ebert, U., Falcke, H., Hörandel, J., Leijnse, H., Mitra, P., et al.: LOFAR lightning imaging: Mapping lightning with nanosecond precision, Journal of Geophysical Research: Atmospheres, 123, 2861–2876, 2018.

Hare, B., Scholten, O., Dwyer, J., Trinh, T., Buitink, S., Ter Veen, S., Bonardi, A., Corstanje, A., Falcke, H., Hörandel, J., et al.: Needle-like structures discovered on positively charged lightning branches, Nature, 568, 360–363, 2019.

Heistermann, M., Jacobi, S., and Pfaff, T.: Technical Note: An open source library for processing weather radar data (ωradlib), Hydrology and Earth System Sciences, 17, 863–871, https://doi.org/10.5194/hess-17-863-2013, 2013.

Hersbach, H., Bell, B., Berrisford, P., Biavati, G., Horányi, A., Muñoz Sabater, J., Nicolas, J., Peubey, C., Radu, R., Rozum, I., et al.: ERA5 hourly data on single levels from 1940 to present, Copernicus climate change service (c3s) climate data store (cds), 10, 2023.

Holmlund, K., Grandell, J., Schmetz, J., Stuhlmann, R., Bojkov, B., Munro, R., Lekouara, M., Coppens, D., Viticchie, B., August, T., et al.: Meteosat Third Generation (MTG): Continuation and innovation of observations from geostationary orbit, Bulletin of the American Meteorological Society, 102, E990–E1015, 2021.

Kumjian, M. R.: Principles and Applications of Dual-Polarization Weather Radar. Part I: Description of the Polarimetric Radar Variables., Journal of Operational Meteorology, 1, 2013a.

Kumjian, M. R.: Principles and Applications of Dual-Polarization Weather Radar. Part II: Warm-and Cold-Season Applications., Journal of Operational Meteorology, 1, 2013b.

Lakshmanan, V. and Witt, A.: Detection of bounded weak echo regions in meteorological radar images, in: Proceedings of 13th International Conference on Pattern Recognition, vol. 3, pp. 895–899, IEEE, 1996.

Liu, N. Y., Scholten, O., Hare, B. M., Dwyer, J. R., Sterpka, C. F., Kolmašová, I., and Santolík, O.: LOFAR observations of lightning initial breakdown pulses, Geophysical Research Letters, 49, e2022GL098 073, 2022.

https://doi.org/10.5194/egusphere-2025-6253
Preprint. Discussion started: 19 January 2026

MacGorman, D. R., Elliott, M. S., and DiGangi, E.: Electrical discharges in the overshooting tops of thunderstorms, Journal of Geophysical Research: Atmospheres, 122, 2929–2957, 2017.

Mak, H. Y. L. and Unal, C.: Peering into the heart of thunderstorm clouds: insights from cloud radar and spectral polarimetry, Atmospheric Measurement Techniques, 18, 1209–1242, 2025.

Mareev, E. A. and Dementyeva, S. O.: The role of turbulence in thunderstorm, snowstorm, and dust storm electrification, Journal of Geophysical Research: Atmospheres, 122, 6976–6988, 2017.

Markowski, P. and Richardson, Y.: Mesoscale meteorology in midlatitudes, John Wiley & Sons, 2011.

Marzano, F. S., Scaranari, D., Celano, M., Alberoni, P., Vulpiani, G., and Montopoli, M.: Hydrometeor classification from dual-polarized weather radar: extending fuzzy logic from S-band to C-band data, Advances in Geosciences, 7, 109–114, 2006.

Mazur, V.: Principles of lightning physics, IoP Publishing, 2016.

Musil, D. J., Heymsfield, A. J., and Smith, P. L.: Microphysical characteristics of a well-developed weak echo region in a High Plains supercell thunderstorm, Journal of Applied Meteorology and Climatology, 25, 1037–1051, 1986.

ωradlib: 2-dimensional membership functions for C-band hydrometeor classification, https://github.com/wradlib/wradlib-data/blob/main/misc/msf_cband_v2.nc, https://github.com/wradlib/wradlib-data/blob/main/misc/msf_cband_v2.nc, netCDF data file, 2024.

Overeem, A., Uijlenhoet, R., and Leijnse, H.: Full-year evaluation of nonmeteorological echo removal with dual-polarization fuzzy logic for two C-band radars in a temperate climate, Journal of Atmospheric and Oceanic Technology, 37, 1643–1660, 2020.

Pedregosa, F., Varoquaux, G., Gramfort, A., Michel, V., Thirion, B., Grisel, O., Blondel, M., Prettenhofer, P., Weiss, R., Dubourg, V., et al.: Scikit-learn: Machine learning in Python, the Journal of machine Learning research, 12, 2825–2830, 2011.

Scholten, O., Hare, B., Dwyer, J., Liu, N., Sterpka, C., Buitink, S., Corstanje, A., Falcke, H., Huege, T., Hörandel, J., et al.: Distinguishing features of high altitude negative leaders as observed with LOFAR, Atmospheric Research, 260, 105 688, 2021a.

Scholten, O., Hare, B., Dwyer, J., Liu, N., Sterpka, C., Buitink, S., Huege, T., Nelles, A., and ter Veen, S.: Time resolved 3D interferometric imaging of a section of a negative leader with LOFAR, Physical Review D, 104, 063 022, 2021b.

Scholten, O., Hare, B., Dwyer, J., Liu, N., Sterpka, C., Kolmašová, I., Santolík, O., Lán, R., Uhlíř, L., Buitink, S., et al.: A distinct negative leader propagation mode, Scientific Reports, 11, 16 256, 2021c.

Scholten, O., Hare, B., Dwyer, J., Sterpka, C., Kolmašová, I., Santolík, O., Lan, R., Uhlíř, L., Buitink, S., Corstanje, A., et al.: The initial stage of cloud lightning imaged in high-resolution, Journal of Geophysical Research: Atmospheres, 126, e2020JD033 126, 2021d.

Scholten, O., Hare, B. M., Dwyer, J., Liu, N., Sterpka, C., Assink, J., Leijnse, H., and Veen, S. t.: Small-Scale Discharges Observed Near the Top of a Thunderstorm, Geophysical Research Letters, 50, e2022GL101 304, https://doi.org/https://doi.org/10.1029/2022GL101304, e2022GL101304 2022GL101304, 2023.

Straka, J. M., Zrnić, D. S., and Ryzhkov, A. V.: Bulk hydrometeor classification and quantification using polarimetric radar data: Synthesis of relations, Journal of Applied Meteorology and Climatology, 39, 1341–1372, 2000.

van Haarlem, M. P., Wise, M. W., Gunst, A., Heald, G., McKean, J. P., Hessels, J. W., de Bruyn, A. G., Nijboer, R., Swinbank, J., Fallows, R., et al.: LOFAR: The low-frequency array, Astronomy & astrophysics, 556, A2, 2013.

van Loon, R.: Research code, https://doi.org/10.5281/zenodo.17948994, gitHub repository, archived via Zenodo, 2025.

Vulpiani, G., Montopoli, M., Passeri, L. D., Gioia, A. G., Giordano, P., and Marzano, F. S.: On the use of dual-polarized C-band radar for operational rainfall retrieval in mountainous areas, Journal of Applied Meteorology and Climatology, 51, 405–425, 2012a.

Vulpiani, G., Montopoli, M., Passeri, L. D., Gioia, A. G., Giordano, P., and Marzano, F. S.: On the use of dual-polarized C-band radar for operational rainfall retrieval in mountainous areas, Journal of Applied Meteorology and Climatology, 51, 405–425, 2012b.

https://doi.org/10.5194/egusphere-2025-6253
Preprint. Discussion started: 19 January 2026

Wang, Y. and Chandrasekar, V.: Algorithm for estimation of the specific differential phase, Journal of Atmospheric and Oceanic Technology, 26, 2565–2578, 2009.

Weisman, M. L.: Bow echoes: A tribute to TT Fujita, Bulletin of the American Meteorological Society, 82, 97–116, 2001.

Zrnić, D. S., Ryzhkov, A., Straka, J., Liu, Y., and Vivekanandan, J.: Testing a procedure for automatic classification of hydrometeor types, Journal of Atmospheric and Oceanic Technology, 18, 892–913, 2001.

https://doi.org/10.5194/egusphere-2025-6253
Preprint. Discussion started: 19 January 2026

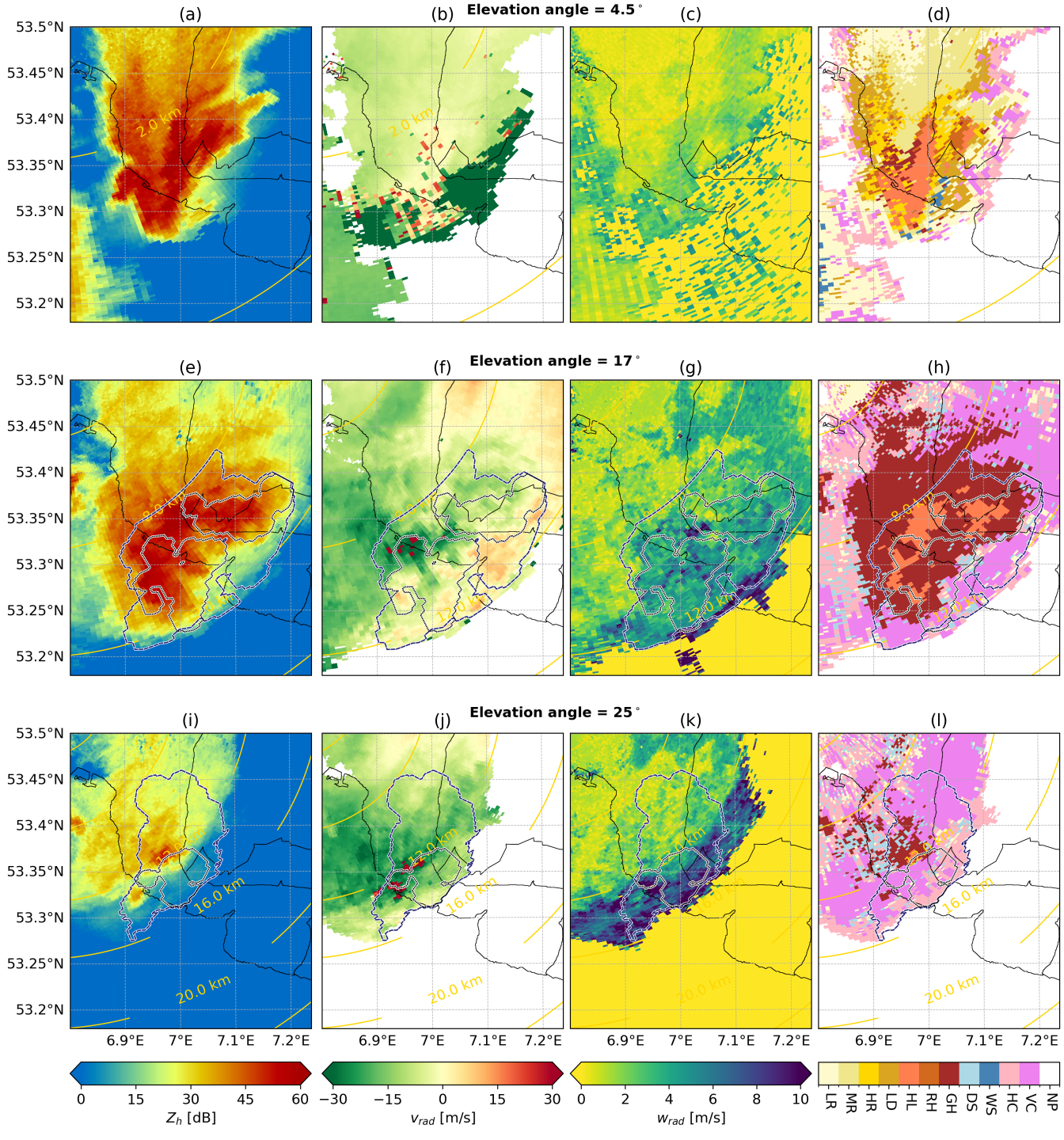

Figure D1. Similar to Fig. 9, but comparing different radar elevation angles (4.5°, 17°, and 25° in rows 1–3 respectively). Panels in the same column share the same variable (Z_h, V_{rad}, W_{rad}, and HMC) and color bar at the bottom.

https://doi.org/10.5194/egusphere-2025-6253
Preprint. Discussion started: 19 January 2026

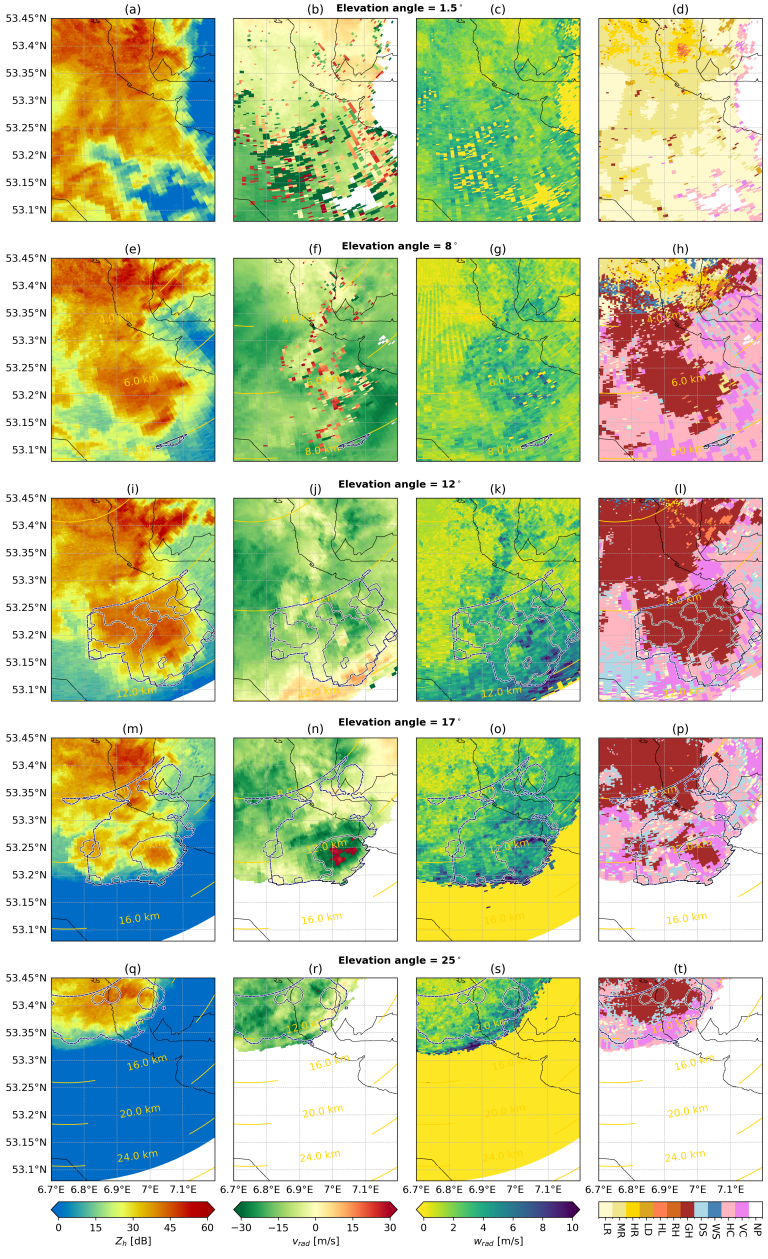

Figure D2. Similar to Fig. 10 and Fig. 10, but comparing different radar elevation angles (1.5°, 8°, 12°, 17°, and 25° in rows 1–5 respectively). Panels in the same column share the same variable (Z_h, V_{rad}, W_{rad}, and HMC) and color bar at the bottom.